Title

Yeast PRPP amidotransferase assembles into fine granules to promote *de novo* purine synthesis through intermolecular substrate channeling

Masak Takaine[1,2], Rikuri Morita[3]

[1]GIAR and [2]IMCR, Gunma University, Maebashi, Japan; [3]Center for Computational Sciences, University of Tsukuba, Ibaraki, Japan

Keywords: purine biosynthesis, *de novo* purine synthesis, PRPP amidotransferase (PPAT), Ade4, yeast

*Correspondence should be addressed to: masaktakaine@gunma-u.ac.jp (M.T.)

Highlights

- Budding yeast PRPP amidotransferase (PPAT) forms intracellular dynamic granules in response to the deprivation of environmental purine bases.
- The assembly of PPAT granules is driven by ribosome crowding in the cytoplasm induced by TORC1.
- Pure PPAT proteins condensate into granule-sized particles *in vitro* under molecular crowding conditions.
- The interaction of PPAT with purine nucleotides prevents granule assembly.
- The condensation of PPAT in granules permits the intermolecular channeling of intermediates, thereby facilitating *de novo* purine synthesis.

Summary

De novo purine synthesis (DPS) is up-regulated under conditions of high purine demands to ensure the mass production of genetic materials and chemical energy, thereby supporting cell proliferation. However, the mechanisms by which DPS is activated remain unclear. We herein demonstrated that PRPP amidotransferase (PPAT), the rate-limiting enzyme in DPS, condensated into granules in *Saccharomyces cerevisiae* cells under purine-depleted conditions. The assembly of granules required phase separation driven by target of rapamycin complex 1 (TORC1)-induced ribosome biosynthesis. A biochemical analysis revealed that the self-assembly of PPAT molecules accounted for granule formation and submillimolar levels of purine nucleotides inhibit self-assembly. Cells unable to form PPAT granules showed growth defects, indicating the physiological importance of granules for the promotion of DPS. These results suggest that the condensation of PPAT by phase transition is a mechanism that regulates DPS sensitively responding to both TORC1 activity and cellular purine demands.

Introduction

Purine nucleotides and their derivatives are involved in many cellular processes and, thus, are essential metabolites for every living organism. The purine nucleotide triphosphates ATP and GTP serve as the energy currencies of cells. Purine metabolites are also incorporated into genetic material, namely, DNA and RNA, as well as coenzymes, such as NAD and coenzyme A. Purine nucleotides are synthesized via both salvage and *de novo* pathways. In mammalian cells, as long as extracellular purine bases are available, purine nucleotides are preferentially synthesized from the recycling of bases through the salvage pathway[1]. Under the condition of a high purine demand (*e.g.*, in actively proliferating cells), the *de novo* pathway is activated to supply higher levels of purine nucleotides[1]. Disorders in the regulation of purine metabolism are associated with various diseases, such as cancer, hyperuricemia (gout), and immunological defects [2, 3]. A more detailed understanding of the regulatory mechanisms underlying purine metabolism will provide insights into the molecular basis of these diseases and facilitate the identification of their therapeutic targets.

The *de novo* purine biosynthetic pathway comprises ten highly conserved sequential chemical reactions that are performed by six enzymes and transforms phosphoribosyl pyrophosphate (PRPP) into inosine 5′-monophosphate (IMP). IMP is subsequently converted into adenosine 5′-monophosphate (AMP) or guanine 5′-monophosphate (GMP) via two branched paths (Fig. 1H). Among these enzymes, only the activity of PRPP amidotransferase (PPAT) (EC 2.4.2.14) is regulated by purine nucleotides [4]. Therefore, PPAT is presumed to be the rate-limiting enzyme in the pathway and plays an important role in the regulation of *de novo* purine synthesis. PPAT catalyzes the first step of the *de novo* pathway, namely, the transfer of amino groups from glutamine onto PRPP to produce 5-phosphoribosylamine (PRA) (eq. 1). This reaction is further divided into two half-reactions: the deprivation of ammonia (NH_3) from glutamine (eq. 2) and the ligation of NH_3 with PRPP (eq. 3). PPAT is a bifunctional enzyme with two catalytic domains: an N-terminal glutamine amidotransferase (GATase) domain that catalyzes the former reaction and a C-terminal phosphoribosyltransferase (PRTase) domain that catalyzes the latter reaction.

$$\mathbf{PRPP + glutamine + H_2O \rightarrow PRA + glutamate + PP_i} \quad \text{(eq. 1)}$$

$$\mathbf{glutamine + H_2O \rightarrow NH_3 + glutamate} \quad \text{(eq. 2)}$$

$$\mathbf{PRPP + NH_3 \rightarrow PRA + PP_i} \quad \text{(eq. 3)}$$

The enzymatic properties and catalytic mechanisms of PPAT have been extensively investigated for decades mainly using enzymes purified from *Escherichia coli* [5] and *Bacillus subtilis* [6]. One of the important features of this enzyme is feedback inhibition by the end-products of the *de novo* pathway, such as AMP and GMP [5-7]. The feedback inhibition of PPAT has been implicated in the suppression of *de novo* purine synthesis in the presence of extracellular salvageable purine bases (and its activation in purine starvation) in mammalian culture cells [7]. Moreover, in the budding yeast *Saccharomyces cerevisiae* and filamentous fungus *Ashbya gossypii*, the expression of PPAT is repressed by the presence of extracellular purine bases [8, 9].

Although the feedback inhibition of PPAT by purine nucleotides appears to play a pivotal role in the regulation of purine synthesis, millimolar levels of AMP or GMP are required for the inhibition of PPAT activity[5, 7, 9]. Intracellular concentrations of AMP and GMP are estimated to be 40–80 and 10–20 μM, respectively, in yeast or mammalian cells under nutrient-rich conditions[10]. The 10- to 100-fold difference between physiological and inhibitory concentrations of AMP and GMP raises the question whether the feedback inhibition of PPAT is directly relevant to the regulation of purine synthesis *in vivo*. Other layers of regulation of PPAT activity, such as post-translational modifications and intracellular signaling, may be involved; however, this has not yet been investigated.

A growing body of evidence reveals that many metabolic enzymes form condensates in cells in response to external stimuli in order to regulate cellular metabolism [11]. For example, the pyruvate kinase Cdc19 in budding yeast reversibly aggregates into large foci upon glucose starvation and heat shock [12, 13]. The assembly of foci protects Cdc19 from stress-induced degradation and inactivates the enzyme, both of which are important for the efficient formation of stress granules and the regrowth of cells after stress relief. Cytidine triphosphate synthase (CTPS) forms filamentous structures in bacteria, yeast, human, and fly germline cells [14-17]. Bacterial CTPS polymerizes into filaments corresponding to the inactive state of the enzyme, while the polymerization of human CTPS into filaments activates the enzyme [18, 19]. PPAT also reversibly localizes to cytoplasmic condensates upon the depletion of extracellular purine bases in budding yeast and HeLa cells [20, 21]. In the case of HeLa cells, PPAT colocalizes with five other enzymes involved in *de novo* purine synthesis in condensates. This multi-enzyme cellular complex is called a purinosome. The molecular basis that regulates the assembly of these PPAT condensates and the physiological importance of the condensates remain unclear.

111 We herein demonstrated that PPAT formed dynamic intracellular granules through phase
112 separation in budding yeast cells in the absence of external purine bases. Active ribosome
113 synthesis promoted by target of rapamycin complex 1 (TORC1) is essential for the
114 molecular crowding of the cytoplasm harnessed to drive phase transition. A biochemical
115 analysis demonstrated that PPAT by itself was sufficient for the assembly of granules, and
116 purine nucleotides at submillimolar concentrations may suppress their assembly.
117 Furthermore, we found that the formation of PPAT granules was important for *de novo*
118 purine synthesis to promote cell proliferation under purine-depleted conditions.
119 Consistent with this result, a computer simulation supported the possible condensation-
120 dependent activation of the enzyme. Collectively, the present results suggest that the
121 condensation of PPAT by phase transition is a mechanism that quickly regulates purine
122 synthesis in response to both TORC1 activity and the concentrations of purine nucleotides.

Results

The yeast phosphoribosylpyrophosphate amidotransferase Ade4 concentrates in fine granules

We visualized the localization of the Ade4 protein, the yeast PPAT, by C-terminally tagging the chromosomal *ADE4* gene with a single yeast codon-optimized GFP (hereafter referred to as GFP). As demonstrated in previous studies [20, 22], Ade4-GFP showed a large focus in cells transferred into medium lacking purine bases, but not in the presence of purine bases (Figs. 1A and 1S1A). However, Ade4-mGFP, Ade4 tagged with a GFP bearing the monomeric mutation A206K[23], appeared as numerous fine dim dots under the same conditions. Ade4-monomeric NeonGreen (mNG) also formed fine granules, but with markedly higher fluorescence intensities (Fig. 1A-B). Moreover, Ade4 tagged with the monomeric red fluorescent protein mKate2 (Ade4-mKate2) showed similar granule localization (Fig. 1S1B). Therefore, we concluded that Ade4-GFP concentrated into 1-2 foci through the dimerization of the GFP moiety. In subsequent experiments, we mainly examined the granules of Ade4-mNG to elucidate the molecular mechanisms regulating the condensation of Ade4 molecules. In some cases, we examined the assembly of Ade4-GFP foci because they basically have the same properties as Ade4-mNG granules and are easily detectable under a microscope because they are brighter than granules and, thus, are suitable for high-content imaging. A close examination of Ade4-mNG granules revealed that they were highly motile and localized throughout the cytoplasm (Fig. 1C). Moreover, time-lapse imaging revealed that the granules were a dynamic structure: they assembled within 40 min after the depletion of an extracellular purine base (adenine) (Figs. 1D, F and 1S1C, and Movies S1-S3) and disassembled within 10 min after supplementation with adenine (Figs. 1E, G and 1S1D, and Movies S4-S6).

Ade4 granules have liquid-like properties

The reversible assembly and dynamic nature of Ade4-mNG granules prompted us to speculate that they are liquid-like assemblies rather than static, solid-like aggregates. Therefore, we treated cells having Ade4-mNG with the aliphatic alcohol 1,6-hexanediol, which is known to dissolve a range of intracellular membrane-less structures [24]. The permeabilization of yeast cells by digitonin did not affect the assembly of Ade4-mNG granules, whereas the granules significantly disassembled within 10 min when exposed to 10% 1,6-hexanediol plus digitonin, revealing their liquid-like properties (Fig. 2A-B).

Previous findings suggested the importance of an intrinsically disordered region (IDR) in

159 the formation of intracellular membrane-less structures[25]. Therefore, we examined the
160 amino acid sequences of Ade4 and other PPATs using the DISOPRED algorithm[26], which
161 predicts IDR using a neural network-based method. We identified an IDR at the C
162 terminus of Ade4 (Fig. 2C). The C-terminal IDR was highly conserved in Ade4
163 homologues of Ascomycota and whole fungi (Fig. 2S1). It was also conserved in the
164 PPATs of species in other kingdoms, particularly those in bacteria and mammals (Fig.
165 2S2). On the other hand, the amino acid sequences of IDRs vary across species, even in
166 yeasts (Fig. 2S3). A mNG-tagged Ade4 mutant lacking the IDR, Ade4ΔIDR-mNG, was
167 incapable of forming granule-like structures, suggesting that the IDR is required for the
168 assembly of Ade4 granules (Fig. 2D). Taken together, these results suggest that Ade4
169 molecules condensate into fine motile granules through IDR-dependent phase separation.
170

171 Formation of Ade4 granules requires active TORC1 and ribosome biogenesis

172 We examined the factors required for phase separation, which drives the assembly of
173 Ade4 granules. During the course of this study, TORC1 has been suggested to control
174 phase separation in the cytoplasm of yeast and mammalian cells by tuning ribosome
175 crowding[27]. Therefore, we investigated whether TORC1 plays a role in the formation of
176 Ade4 granules. In cells, rapamycin has been shown to bind to FKBP12, and this complex
177 potently inhibited TORC1[28]. The addition of rapamycin suppressed the assembly of
178 Ade4-GFP foci in wild-type cells, while rapamycin did not affect the foci in cells lacking
179 Fpr1 (budding yeast FKBP1) (Fig. 3A). Rapamycin also significantly suppressed the
180 assembly of Ade4-mNG granules in wild-type cells (Fig. 3B-C). These results suggested
181 that the activity of TORC1 was necessary for the assembly of Ade4 granules. To further
182 identify the TORC1-related factors responsible for Ade4 granule formation, we observed
183 Ade4-GFP foci in 37 single-gene deletion mutants, each of which lacked one of the 17
184 upstream regulators, the 17 downstream effectors of TORC1 signaling, or 3 genes of
185 interest (Fig. 3S1A-B). Consistent with the inhibitory effects of rapamycin, the assembly
186 of Ade4-GFP foci was liable to be attenuated in mutants of the upstream activators of
187 TORC1 signaling (such as the Pib2 or EGO complex). Most of the downstream effectors
188 of TORC1 signaling appeared to have no or only a negligible effect on Ade4-GFP foci.
189 However, the assembly of the foci and granules of Ade4-mNG was significantly
190 suppressed in *sfp1*Δ and *sit4*Δ cells (Figs. 3D-E and 3S1A-B).
191

192 Sfp1 and Sit4 have both been implicated in cytoplasmic crowding through ribosome
193 biogenesis [27, 29, 30]. Therefore, we examined the importance of ribosome synthesis on Ade4
194 granule formation. Diazaborine has been shown to specifically inhibit the maturation of

195 the 60S ribosomal subunit and reduce the level of the 60S subunit in yeast cells [31]. The
196 treatment of cells with diazaborine strongly suppressed the formation of Ade4-GFP foci
197 and Ade4-mNG granules, suggesting that the active synthesis of the ribosomal 60S
198 subunit is required for the assembly of these condensates (Figs. 3F and 3S1C-D). Taken
199 together, macromolecular crowding of the cytoplasm by TORC1-mediated ribosome
200 synthesis may be the main driving force of phase separation required for the assembly of
201 Ade4 granules.
202

203 Intracellular derivatives of purine nucleotides prevent the formation of Ade4
204 condensates

205 Although phase separation driven by macromolecular crowding in the cytoplasm was
206 necessary for the assembly of Ade4 granules, it was only one of the prerequisites. Another
207 layer of regulation is required to enable cells to suppress the assembly of granules in the
208 presence of extracellular purine bases. Purine bases are actively transported into cells by
209 the purine-cytosine permease Fcy2[32] and converted to various metabolites (Fig. 4A).
210 Therefore, we investigated the metabolites responsible for the suppression of Ade4
211 granule formation. Foci were dissolved in wild-type cells with Ade4-GFP foci treated
212 with medium containing adenine or hypoxanthine (Fig. 4B-E, wt). In *aah1*Δ*apt1*Δ cells,
213 in which incorporated adenine was not further metabolized, the addition of hypoxanthine,
214 but not adenine, dissolved Ade4 foci (Fig. 4B-C). These results suggested that
215 intracellular adenine itself did not affect Ade4 granules. In *hpt1*Δ cells in which
216 incorporated hypoxanthine was not further metabolized, the addition of hypoxanthine did
217 not disassemble Ade4 foci, whereas the addition of adenine slightly dissolved the foci
218 (Fig. 4B, D). This result indicated that intracellular hypoxanthine itself did not affect
219 Ade4 granules, and also that intracellular adenine was efficiently converted to
220 hypoxanthine. In *ade12*Δ cells in which IMP was not converted to AMP via
221 adenylosuccinate (S-AMP), the addition of hypoxanthine did not disassemble Ade4 foci,
222 whereas that of adenine moderately dissolved the foci (Fig. 4B, E). The inhibition of
223 Ade12 by alanosine, a specific inhibitor of adenylosuccinate synthetase [33], gave similar
224 results: in alanosine-treated cells, the addition of hypoxanthine partially dissolved Ade4-
225 GFP foci (Fig. 4S1A-C). Based on these results, we concluded that adenine nucleotides,
226 including S-AMP derived from external purine bases, were responsible for inhibiting the
227 assembly of Ade4 condensates in the presence of extracellular purine bases.
228

229 Interaction of purine nucleotides with Ade4 is implicated in granule assembly

230 We initially suspected that Ade4 itself was the site of action of the inhibitory adenine

231 nucleotide suppressing its granule assembly because PPATs have been shown to directly
232 bind to purine nucleotides, particularly AMP and GMP [1, 6, 34]. Interactions with these
233 purine nucleotides down-regulate PPATs (see the Introduction). A structural analysis of *B.*
234 *subtilis* PPAT proposed the involvement of K316 and R318 in interactions with adenine
235 nucleotides (Fig. 5A), and the replacement of these residues with glutamine reduced
236 affinity for AMP or GMP[35 34]. Furthermore, D293 has been suggested to interact with
237 purine nucleotides, and the replacement of the residue with valine reduced affinity for
238 purine nucleotides[9]. Structural data showed that these three amino acids formed hydrogen
239 bonds with ADP or GMP (Fig. 5A). These three amino acid residues, and their adjacent
240 amino acid sequences, were well conserved among the PPATs of various species,
241 including budding yeast (Fig. 5B). Therefore, we introduced these corresponding
242 mutations into Ade4 (D310V, K333Q, and R335Q, hereafter Ade4-VQQ) and assessed
243 whether the interaction with purine nucleotides affected the assembly of Ade4 granules.
244 In comparisons with the granules of Ade4-mNG, those of Ade4-VQQ-mNG were
245 detected in a higher percentage of cells (Fig. 5C, D) and had a higher fluorescence
246 intensity (Fig. 5E). These results suggested that the mutant Ade4 was more liable to
247 assemble and condense into granules. In other words, the binding of purine nucleotides
248 to Ade4 may play an inhibitory role in granule assembly.
249

250 ## Ade4 protein condensates into particles under molecular crowding conditions *in*
251 *vitro*

252 Regarding the molecular mechanisms regulating the assembly of Ade4 granules, two
253 mutually exclusive possibilities appeared. The first possibility was that Ade4 itself was
254 sufficient for granule assembly, and the second was that other cellular components
255 (including proteins, lipids, and organelles) were required to assemble Ade4 into granules.
256 To distinguish the two possibilities, we investigated the properties of the pure Ade4
257 protein *in vitro*. A previous study reported that the expression of Ade4 in the active form
258 was negligible in bacteria [36]. Therefore, we purified Ade4-mNG from budding yeast cells
259 (Fig. 6S1A). Using data derived from twenty quantitative proteomic studies, intracellular
260 concentrations of Ade4 were estimated to be approximately 0.5 μM (Fig. 6S2). In
261 subsequent *in vitro* assays, we selected the concentrations of Ade4-mNG that were close
262 to or slightly lower than the estimated concentration. Under physiological ionic
263 conditions (0.15 M NaCl, 4 mM $MgCl_2$, pH 7.5), purified Ade4-mNG homogenously
264 dispersed, showing no aggregates ("0%" in Fig. 6A). We then tested the effects of
265 macromolecular crowding using polyethylene glycol (PEG) as a crowding agent. The
266 addition of PEG8000 induced the formation of sub-micron-sized particles of Ade4-mNG

267 in a concentration-dependent manner; a large amount of particles formed in >10% PEG
268 (Fig. 6A-C). The aggregation of the pure mNG protein was not induced by 10% PEG (Fig.
269 6S1B). We also investigated the effects of PEG sizes and found that Ade4-mNG
270 assembled into particles in the presence of >4 kDa PEG (Fig. 6S1C). Consistent with this
271 size dependency, other crowding agents, 2% lysozyme (MW: 14 kDa) and Ficoll-400
272 (MW: 400 kDa) induced the assembly of Ade4-mNG particles (Fig. 6S1F). These results
273 clearly suggested that Ade4 by itself was capable of assembling into sub-micron particles
274 under macromolecular crowding conditions.
275
276 We then examined the role of phase separation in the self-assembly of Ade4-mNG *in vitro*.
277 In the presence of 1, 6-hexanediol, the mean fluorescence intensity and total mass of
278 Ade4-mNG particles were both significantly reduced (Fig. 6D-F). Similarly, Ade4ΔIDR-
279 mNG self-assembled into particles less effectively than Ade4-mNG (Fig. 6G-I).
280 Therefore, we concluded that Ade4 molecules partially aggregated independently of the
281 IDR moiety, and phase separation was important for the full assembly of Ade4 particles
282 *in vitro*.
283
284 Purine nucleotides attenuate the assembly of Ade4 particles *in vitro*
285 As demonstrated above, purine nucleotides were expected to suppress the aggregation of
286 Ade4 in yeast cells (Figs. 4 and 5). Therefore, we investigated whether purine nucleotides
287 exerted some effects on the *in vitro* assembly of Ade4-mNG particles. In the presence of
288 GMP, AMP, ADP, and ATP, the condensation of Ade4-mNG was significantly reduced
289 (Fig. 7A and Fig. 7S1C). AMP, ADP, and ATP were more effective than GMP, while S-
290 AMP unexpectedly had no significant effect. Adenine and inosine, a degradation product
291 of IMP, did not affect the *in vitro* condensation of Ade4 (Fig. 7S1A-B), which is consistent
292 with *in vivo* results (Fig. 4). More than 250 μM AMP, ADP, or ATP was required to
293 achieve maximal inhibitory effects, whereas the inhibitory effects of GMP plateaued at
294 100 μM (Fig. 7B-D and Fig. 7S1D). Importantly, AMP also inhibited the condensation of
295 Ade4ΔIDR-mNG as well as that of Ade4-mNG (Fig. 7E). These results suggested that
296 purine nucleotides, including AMP, ADP, ATP, and GMP, repressed the condensation of
297 Ade4 molecules by inhibiting IDR-independent aggregation.
298
299 Formation of Ade4 granules is important for efficient *de novo* purine synthesis
300 during cell growth
301 We examined the physiological significance of Ade4 granules. On solid medium in the
302 absence of adenine, the growth of cells expressing Ade4ΔIDR-3HA, which failed to

303 assemble into granules, was markedly slowly than those expressing Ade4-3HA (Fig. 8A).
304 The protein level of Ade4ΔIDR-3HA in cells grown in adenine-free medium was similar
305 to that of Ade4-3HA (Fig. 8B). Supplementation with adenine restored the growth of the
306 *ADE4ΔIDR* mutant to the wild-type rate, indicating that the slow growth of the mutant
307 was due to the limited activity of the enzyme and not to dominant-negative inhibition
308 caused by the mutant protein. We also noted that the phenotype of the *ADE4ΔIDR* mutant
309 depended on the nitrogen source of the medium: the mutant grew more slowly as
310 concentrations of ammonium ions in the medium decreased (Fig. 8A). Therefore, we
311 quantitatively examined cell growth by measuring growth curves in liquid medium. The
312 *ADE4ΔIDR* mutant showed significantly slower growth, particularly in the absence of
313 ammonium ions, whereas the growth rate of the wild-type strain was almost independent
314 of ammonium ion concentrations in the medium (Fig. 8C-D and Fig. 8S1A-B). These
315 results suggested that the formation of Ade4 granules was important for enhancing
316 enzymatic activities in cells to support efficient cell growth, particularly in a low-
317 ammonium environment.
318
319 Biochemical analyses previously revealed that PPAT directly utilized NH_3 as a nitrogen
320 donor in place of glutamine to produce PRA[5]. Glutamine-dependent PRA synthesis (Gln-
321 PRA activity) (Fig. 8S1C) and NH_3-dependent PRA synthesis (NH_3-PRA activity) (Fig.
322 8S1C) have both been implicated in the *de novo* biosynthesis of purine nucleotides *in vivo*
323 [37 38]. Moreover, biochemical assays revealed that NH_3-PRA activity depended on the
324 concentrations of NH_4Cl, a fraction of which was in the form of NH_3, whereas Gln-PRA
325 activity was inhibited by NH_3 [5]. Therefore, Gln-PRA activity and NH_3-PRA activity may
326 be activated in cells under low and high NH_3 (ammonium) conditions, respectively (Fig.
327 8S1C-D). We speculated that the slow ammonium concentration-dependent growth of the
328 granule-hypoplasia *ADE4ΔIDR* mutant was due to the inefficient enhancement of the
329 Gln-PRA activity of Ade4.
330
331 MD calculations predict the possible leakage of glutamine-derived NH_3 from
332 PPAT molecules
333 In the process of PRA synthesis from glutamine, NH_3 is drawn from glutamine at the first
334 glutamine amidotransferase (GATase) site and then needs to be efficiently transferred to
335 PRPP loaded on the second phosphoribosyltransferase (PRTase) site to prevent the release
336 of intermediate NH_3 into bulk solution. A structural analysis of *E. coli* PPAT suggested
337 that the binding of PRPP activated PPAT and resulted in the formation of a hydrophobic
338 channel connecting the GATase and PRTase sites [39]. Therefore, the channel was expected

339 to permit the efficient intramolecular transfer of the intermediate NH_3 between the two
340 catalytic sites (Figs. 9F, H and 9S1A). However, we hypothesized that the extreme
341 condensation of granules enabled the intermolecular transfer of the intermediate NH_3
342 between Ade4 molecules and, hence, promoted Gln-PRA activity. Therefore, we
343 investigated whether glutamine-derived NH_3 escaped from the initial site through paths
344 other than the intramolecular channel by examining the behavior of NH_3 on the PPAT
345 molecule using a molecular dynamics (MD) simulation. The calculation of MD was based
346 on the crystal structure of *E. coli* PPAT in the active form (PDB: 1ECC) [39].
347
348 We performed MD simulations for the holo condition of PPAT that contained glutamic
349 acid, NH_3, PRPP, and Mg^{2+}. During ten individual trials, NH_3 was not released from PPAT
350 and remained in the initial or adjacent positions (Fig. 9A). NH_3 did not reach the catalytic
351 site. We then performed MD simulations for the semi-holo condition that contained only
352 glutamic acid and NH_3. NH_3 was released through the hydrophobic channel once in the
353 ten trials. NH_3 was released through a transient channel that was directed to Arg333,
354 which was conserved in Ade4, hereinafter referred to as the front channel, four times in
355 ten trials (Fig. 9B, D). Prior to the release of NH_3, a hydrophobic side chain of Phe260
356 was flipped from the initial structure. Furthermore, Arg333 functioned as a gate for NH_3
357 and water by forming hydrogen bonds with the backbone oxygen of Tyr259, Phe260,
358 His26, and the phosphate group of PRPP (Fig. 9D, E). In the semi-holo condition, the
359 lack of PRPP opened the Arg gate. To confirm the existence of the Arg gate, additional
360 MD simulations were performed on the Arg333Ala mutant under the holo condition. As
361 expected, the flipping of the Phe260 side chain and NH_3 release were both observed six
362 times in ten trials even though PRPP was in the catalytic site (Fig. 9C).
363
364 These results suggested that after the production of NH_3 from glutamine, the attack of
365 external NH_3 released PRA, which opened the Arg gate, making the front channel, and
366 internal NH_3 then escaped from the channel (Fig. 9G and 9S1C).
367

368 **Discussion**

369 We herein demonstrated that the budding yeast PPAT Ade4 formed intracellular fine
370 granules in purine-depleted media. These granules were highly dynamic and possessed
371 liquid-like properties, and phase separation was involved in granule assembly. We also
372 showed that phase separation was driven by the molecular crowding of the cytoplasm
373 induced by active TORC1 and its downstream ribosome biogenesis. Purified Ade4 self-
374 assembled into sub-micron-sized particles, and sub-millimolar purine nucleotides
375 inhibited the formation of particles, as indicated by the genetic analysis. Cells unable to
376 form Ade4 granules showed slower growth, suggesting the importance of the granules
377 for the promotion of *de novo* purine synthesis. The MD simulation implied the
378 condensation-dependent activation of PPAT by enabling the intermolecular channeling
379 of the intermediate NH_3. These results indicate that the formation of Ade4 granules is a
380 biologically relevant mechanism that regulates purine synthesis in response to both
381 TORC1 activity and purine nucleotide levels.
382
383 We visualized intracellular fine granules of the budding yeast Ade4 using the bright,
384 monomeric fluorescent protein mNG. These structures were overlooked in previous
385 studies in which Ade4 was tagged with non-monomeric GFP[20, 22]. The large foci of
386 Ade4 reported in previous studies and granules appeared to share basic properties;
387 however, since the pure Ade4 protein assembles into granule-sized particles, the latter is
388 likely to be the actual structure of Ade4. A close examination of granules revealed their
389 inherently dynamic nature in that they quickly assembled or disassembled in response to
390 environmental purine bases.
391
392 A previous study demonstrated that Ade4 played an indirect, but pivotal role in
393 regulating the expression of AMP biosynthesis genes in response to extracellular purine
394 bases [36]. The present results suggest that Ade4 is also crucial for the more rapid, short-
395 term regulation of purine biosynthesis, in addition to its long-term regulation at the
396 transcriptional level.
397

398 Assembly mechanism of Ade4 granules

399 We found that phase separation dependent on both TORC1 activity and the C-terminal
400 IDR of Ade4 was essential for the assembly of Ade4 granules. In addition, we identified
401 Sfp1 and Sit4 as genes downstream of TORC1 that are critically involved in granule
402 assembly. Since both genes are important for ribosome synthesis, the requirement of
403 ribosome synthesis for granule assembly was tested and confirmed. These results are

404 consistent with the theory that TORC1 regulates the macromolecular crowding of the
405 cytoplasm through ribosome synthesis and degradation, which, in turn, controls
406 biomolecular condensation by phase separation [27]. This study is the first experimental
407 demonstration of a metabolic enzyme assembling into condensates by the TORC1-
408 regulated phase transition of the cytoplasm in yeast cells (Figure 7F, left panel). Since
409 TORC1 and PPAT IDRs are both conserved in many species, the condensation of PPAT
410 by TORC1 may be a common feature in eukaryotic cells.
411
412 We successfully purified the Ade4 protein from the budding yeast cells. To our
413 knowledge, this is the first complete purification of a eukaryotic PPAT. Purified Ade4
414 was capable of self-assembling into fine particles under molecular crowding conditions.
415 Therefore, we speculated that Ade4 by itself also assembled into granules in cells;
416 however, unidentified auxiliary factors may participate in their assembly. *In vitro* assays
417 also revealed that the condensation of Ade4 comprised IDR-independent aggregation
418 and IDR-dependent phase separation. The former may be a prerequisite for the latter
419 (Fig. 7F, right panel). IDR-independent aggregates were small and appeared to be
420 unstable in living cells and, hence, were undetectable (Fig. 2D). Phase separation may
421 be required for the stable condensation of aggregates into granules. There was a
422 threshold size and concentration of PEG required to induce the formation of Ade4
423 particles *in vitro*, which suggested that the assembly of Ade4 granules is only allowed
424 within a narrow range of ribosome concentrations *in vivo*.
425
426 The genetic analysis indicated an inhibitory role for purine nucleotides in the assembly
427 of Ade4 granules, and purine nucleotides suppressed the IDR-independent aggregation
428 of Ade4 *in vitro*. Therefore, we speculated that the intracellular purine nucleotide
429 concentration, which fluctuates in response to extracellular purine bases, controlled the
430 assembly of Ade4 granules as another regulatory layer of PPAT activity (Fig. 7F, right
431 panel). Human PPAT has been shown to form an inactive tetramer in complex with
432 AMP, but an active dimer in the apo form. [7, 40]. Moreover, human PPAT bearing a
433 mutation that corresponds to K333Q, one of the VQQ mutations, predominantly formed
434 active dimers, even in the presence of AMP[7]. Therefore, interactions with purine
435 nucleotides are closely associated with the transition between the dimer and tetramer in
436 eukaryotic PPAT. The present results further suggest that dimers (depicted by hexagons
437 on the right in Fig. 7F), but not tetramers (depicted by circles), are prone to aggregate
438 under molecular crowding conditions. This model indicates that the affinity of each
439 purine nucleotide for Ade4 affects the strength of inhibition. Satyanarayana and Kaplan

440 reported that AMP, ADP, and ATP inhibited the enzymatic activity of partially purified
441 Ade4 more strongly than GMP [41], which is consistent with the present results.
442
443 Biological significance of Ade4 granules
444 The condensation of Ade4 into granules is of physiological significance because cells
445 devoid of granules show slower growth as environmental NH_3 levels decrease. This
446 phenotype is suppressed in the presence of purine bases, in which purine synthesis
447 through the salvage pathway is available. This suggests that condensation activates the
448 rate-limiting enzyme Ade4 and, thus, is important for the activation of *de novo* purine
449 synthesis. Under low ammonium conditions, it is more important to use glutamine as a
450 substrate. We hypothesized that condensation promotes the Gln-PRA activity of Ade4.
451 The MD simulation revealed a previously unidentified path through which glutamine-
452 derived intermediate NH_3 leaked out of the PPAT molecule (Figs. 9G and 9S1C). By its
453 nature, the NH_3 molecule rapidly diffuses throughout the cytoplasm. However, in Ade4
454 granules, in which the local concentration of the enzyme is very high, another enzyme
455 was more likely to trap NH_3 and process it by the PRTase domain (Figs. 9H and 9S1D).
456 In other words, since the transfer efficiency of the intermediate NH_3 is not necessarily
457 perfect, the condensation of Ade4 with two catalytic domains is equivalent to the co-
458 clustering of two enzymes having GATase and PRTase, respectively, in the microspace.
459 This type of activation by intermolecular NH_3 channeling corresponds to the clustering-
460 mediated metabolic channeling (of intermediates) theoretically predicted by Castellana
461 et al [42]. They also experimentally confirmed the prediction using artificially clustered
462 enzymes in *E. coli*. The present results provide further evidence that native bifunctional
463 enzymes are activated by the metabolic channeling in eukaryotic cells.
464
465 The activity of PPAT is known to be regulated in a feedback manner by millimolar
466 levels of AMP and GMP *in vivo* [43]. However, since intracellular purine mononucleotide
467 concentrations are generally in the micromolar range of tens to hundreds, this regulation
468 does not appear to be physiologically relevant. The present study elucidated a
469 mechanism that regulates intracellular PPAT activity in a more acute, sensitive, and
470 physiologically valid manner.
471
472 TORC1 is activated by sensing nutrients, such as amino acids, glucose, and ATP [44].
473 Therefore, the requirement of TORC1 activity for PPAT condensation ensures that the
474 *de novo* synthesis of purines is only up-regulated under conditions that are favorable for
475 cell growth. A previous study also reported that mammalian TORC1 transcriptionally

476 up-regulated enzymes involved in the mitochondrial tetrahydrofolate cycle, thereby
477 increasing *de novo* purine synthesis [45]. Correlating the metabolic flux of purine
478 synthesis with the nutritional status via TORC1 activity appears to be a conserved and
479 elaborate strategy for cell proliferation.
480
481 Recent studies showed that many metabolic enzymes formed intracellular condensates
482 by phase separation, allowing cell metabolism to adapt to changing growth conditions.
483 [11]. These condensates were mostly a temporary store of inactive enzymes to survive
484 adverse environmental conditions and, in a few cases, an activated form of enzymes. As
485 already described in the Introduction, human CTPS polymerizes into filaments with an
486 active conformation[18]. Mammalian acetyl-CoA carboxylate 1 (ACC1) has also been
487 shown to form filamentous structures *in vivo* and *in vitro* for decades. A recent study
488 revealed that filament formation in the presence of citrate locked human ACC1 into an
489 active conformation[46]. The present results provide another example where the
490 condensation of a metabolic enzyme leads to its activation. However, Ade4
491 condensation is unique in that it forms highly dynamic structures and activates its
492 enzymatic activity through the cluster-mediated channeling of intermediates. Although
493 Ade4 does not appear to polymerize into filaments, future research is awaited to
494 elucidate the molecular organization within granules. A more detailed understanding of
495 the architecture of PPAT condensates will provide insights into the mechanism of
496 condensation. Based on that information, PPAT condensation has potential as a
497 therapeutic target for diseases associated with abnormal purine metabolism, such as
498 cancer and gout.
499

500 **Materials and Methods**

501 Yeast strains and plasmids

502 The yeast strains, plasmids, and primers used in the present study are listed in
503 Supplementary Tables S1, S2, and S3 respectively. These strains were constructed by a
504 PCR-based method [47] and genetic crosses. The yeast knockout strain collection was
505 originally purchased from GE Healthcare (cat. # YSC1053).
506
507 Regarding the construction of plasmids used for the C-terminal tagging of monomeric
508 GFP or mKate2, DNA fragments encoding the corresponding fluorescent proteins were
509 artificially synthesized (Eurofin Genomics, Ebersberg, Germany). These fragments
510 were replaced with GFP of pYM25[47] using *Sal*I/*Bgl*II sites to yield MTP3114 and
511 MTP3131, respectively. The plasmid used for the C-terminal tagging of mNG-Strep tag
512 II (MTP3139) was constructed in the same manner: a DNA fragment encoding single
513 mNG fused with the Strep II tag (WSHPQFEK) by a spacer sequence (ELYKGSA) was
514 synthesized and then replaced with the GFP of pYM25.
515

516 Media and cell culture

517 Synthetic medium optimized for the growth of the BY strain was prepared as described
518 by Hanscho et al. [48]. Growth assays in solid and liquid media used optimized synthetic
519 media lacking glutamate, phenylalanine, serine, and threonine. Yeast nitrogen base
520 without amino acids, but with ammonium sulfate (cat. # Q30009) was purchased from
521 Invitrogen. Yeast nitrogen base without amino acids and ammonium sulfate (cat. #
522 CYN0501) was purchased from FORMEDIUM. Rich medium was standard YPD
523 medium composed of 1% (w/v) yeast extract (BD, cat. # 212750), 2% (w/v) bacto-
524 peptone (BD, cat. # 211677), and 2% (w/v) D-glucose. Glucose (cat. # 049-31165),
525 adenine sulfate (cat. # 018-10613), hypoxanthine (cat. # 086-03403), 1, 6-hexanediol
526 (cat. # 087-00432), and digitonin (cat. # 043-2137) were purchased from FUJIFILM
527 Wako. Cells were grown to the mid-log phase at 30°C before imaging unless otherwise
528 noted. To replace medium containing adenine with medium lacking adenine, cells were
529 collected in a microtube by brief centrifugation and suspended in medium lacking
530 adenine. This washing procedure was repeated at least twice. Rapamycin was purchased
531 from LC Laboratories (cat. # R-5000).
532

533 Microscopy

534 Cells expressing a GFP-fusion protein were concentrated by centrifugation and
535 sandwiched between a slide and coverslip (No. 1.5 thickness, Matsunami, Osaka,

536 Japan). Immobilized cells were imaged using an inverted fluorescent microscope
537 (Eclipse Ti2-E, Nikon, Tokyo, Japan) equipped with a CFI Plan Apoλ 100× Oil
538 DIC/NA1.45 objective lens and CMOS image sensor (DS-Qi2, Nikon). The fluorescent
539 signal was collected from stacks of 11 *z*-sections spaced by 0.5 μm, and the maximum
540 projections of the optical sections were shown unless otherwise noted. A CFI Plan Apoλ
541 60× Oil Ph3 DM/NA1.40 or CFI Plan Apoλ 100× Oil Ph3 DM/NA1.45 objective lens
542 was used for phase contrast imaging. Images of cells were acquired from several fields
543 of view for each experimental condition. All digital images were processed with the Fiji
544 image platform[49].
545

546 Quantitative analysis of intracellular fluorescent condensation

547 Intracellular fluorescent condensation (*i.e.*, Ade4-GFP foci or Ade4-mNG granules) was
548 automatically detected and analyzed by running Fiji macros
549 (https://github.com/masaktakaine/FP-foci-quantification and
550 https://github.com/masaktakaine/FP-granules-quantification). Briefly, these macro
551 extract cell outlines from phase-contrast images and detect fluorescent condensation
552 inside the cell boundary using the *FindMaxima* function of Fiji software.
553
554 To monitor temporal changes in the number of intracellular Ade4-mNG granules by
555 time-lapse imaging, the number of maxima of green fluorescence intensity in the field
556 was counted in each time frame and divided by the total cell number by running a Fiji
557 macro (https://github.com/masaktakaine/Counting-FP-granules-in-time-lapse).
558 In cases in which phase-contrast images were unavailable, we manually examined
559 condensation.
560

561 Spot growth assay

562 Cells were grown to the mid-log phase at 30°C in synthetic medium, and cell density
563 (cells/ml) was measured by an automated cell counter (TC20, Bio-Rad). The culture
564 was diluted by medium lacking nitrogen and carbon sources to a density of 1×10^6
565 cells/ml, serially diluted 5-fold, and spotted on plates. Plates were incubated for 2-3
566 days at 30°C and then imaged by an image scanner (GT-X830, EPSON).
567

568 Measurement of growth curves in a liquid culture

569 Cell growth in liquid media was monitored in a 96-well flat-bottomed plate using a
570 microplate reader (iMark, Bio-Rad). Cells were grown to the mid-log phase and then

571 diluted to OD_{600} = 0.1. Each well was filled with 300 μl of the cell dilution and OD_{595}
572 was measured at 30°C every 10 min.
573
574 Immunoblot analysis
575 A denatured whole-cell extract was prepared according to the method reported by von der
576 Haar (2007) [50]. Briefly, mid-log cells were harvested from 2–3 ml of the culture by
577 centrifugation. The cell pellet was resuspended in a small volume (<100 μl) of lysis buffer
578 (0.1 M NaOH, 50 mM EDTA, 2% (w/v) SDS, and 2% (v/v) β-mercaptoethanol) and then
579 incubated at 90°C for 10 min. The sample was neutralized by the addition of a one-tenth
580 volume of 1 M acetic acid, incubated at 90°C for 10 min, and mixed with a one-third
581 volume of 4×Laemmli protein sample buffer (cat. # 1610747, Bio-Rad). Following
582 centrifugation at 20,000×*g* at 4°C for 10 min, the upper 90% of the supernatant was
583 collected as the clarified whole-cell extract and stored at -30°C until used. Proteins were
584 resolved by SDS-PAGE using a pre-cast gel containing 10% (w/v) acrylamide
585 (SuperSep™ Ace, cat. # 195-14951, FUJIFILM Wako) and then transferred onto a PVDF
586 membrane (Immobilon-P, Millipore) using a protein transfer system (Trans-Blot Turbo
587 Transfer System, Bio-Rad). HA-tagged Ade4 proteins were detected using an anti-HA
588 antibody (mouse monoclonal (12CA5), cat. # GTX16918, Funakoshi) at a 1:1000 dilution.
589 GFP-tagged proteins were detected using an anti-GFP antibody (mouse monoclonal
590 (1E10H7), cat. #66002-1-Ig, ProteinTech) at a 1:1000 dilution. GAPDH was detected
591 using an anti-GAPDH antibody (mouse monoclonal (1E6D9), cat. # 60004-1-Ig,
592 ProteinTech) at a 1:1000 dilution. PGK1 was detected using an anti-PGK1 antibody
593 (mouse monoclonal (22C5D8), cat. # ab113687, Abcam) at a 1:1000 dilution. An HRP-
594 conjugated secondary antibody (from sheep, cat. #NA931V, GE Healthcare) was probed
595 at a 1:10000 dilution. Immunoreactive bands were luminescent in a chemiluminescent
596 substrate (Western BLoT Quant HRP substrate, cat. # T7102A, TaKaRa) and imaged
597 using an image analyzer (LAS4000, GE Healthcare).
598
599 Protein purification from yeast cells
600 Ade4-mNG, Ade4ΔIDR-mNG, and mNG were C-terminally tagged with a single Strep-
601 tag II, expressed in budding yeast cells, and purified as follows. Yeast cells expressing
602 the tagged protein were grown in liquid YPD medium supplemented with 0.02 mg/ml
603 adenine sulfate at 30°C for at least 20 h. The pre-culture was diluted by 100–1000-fold in
604 100 ml of fresh YPD plus adenine medium, and cells were further grown at 30°C to 4×10^7
605 cells/ml. Cells were harvested by centrifugation at 2,000×*g* and washed twice with 1 ml
606 of extraction buffer (EB) (0.15 M NaCl, 1 mM EDTA, 1 mM dithiothreitol, and 40 mM

607 Tris-HCl, pH 7.5) supplemented with 1 mM PMSF and cOmplete protease inhibitor
608 cocktail (EDTA-free) (Roche, cat. # 11836170001). One gram of glass beads with a
609 diameter of 0.5 mm (YASUI KIKAI, cat. # YGBLA05) was mixed with the cell
610 suspension, and cells were disrupted by vigorous shaking using a beads beater (YASUI
611 KIKAI, MB901). The crude cell extract was collected by brief centrifugation, and glass
612 beads were washed with a small volume of EB (<0.5 ml). The crude extract and washings
613 were combined and clarified by centrifugation twice at 20,000×*g* at 4°C for 10 min. To
614 block endogenous biotin, the cleared lysate was supplemented with 0.2 mg/ml neutralized
615 avidin (FUJIFILM Wako, cat. # 015-24231), incubated on ice for 30 min, and clarified
616 by centrifugation at 20,000×*g* at 4°C for 10 min. The supernatant was loaded onto a
617 handmade open column packed with 0.5 ml of Strep-Tactin Sepharose (IBA GmbH, cat.
618 # 2-1201-002). After washing with 10 column volumes of EB, bound proteins were eluted
619 with 6 column volumes of EB plus 2.5 mM D-desthiobiotin (IBA GmbH, cat. # 2-1000-
620 025). The protein amounts and compositions of elution fractions were analyzed by SDS-
621 10% PAGE and stained with FastGene Q-stain (Nippon Genetics, cat. # NE-FG-QS1).
622 Peak fractions were pooled and concentrated using an Amicon Ultra-0.5 centrifugal filter
623 device with a molecular weight cut-off of 30 or 10 kDa (Merck, cat. # UFC503024 or
624 UFC501008). D-desthiobiotin in the peak fraction was diluted more than 100-fold by a
625 repeating dilution with EB and the centrifugal concentration. The concentration of the
626 purified protein was assessed by densitometry using bovine serum albumin (TaKaRa, cat.
627 # T9310A) as a standard following SDS-PAGE and staining with the Q-stain. Purified
628 Ade4-mNG and Ade4ΔIDR-mNG were supplemented with 5 and 10 mM DTT and stored
629 on ice.
630
631 *In vitro* condensation assay
632 The purified protein was diluted to the indicated concentration in assay buffer (EB plus
633 5 mM $MgCl_2$) and supplemented with 0–15% (w/v) PEG 8000 (FUJIFILM Wako, cat. #
634 596-09755). In the experiments shown in Fig. 6S1C, samples were spiked with 10%
635 (w/v) PEG of the indicated molecular size. The mixture was immediately loaded into an
636 assay chamber composed of a glass slide and coverslip attached by double-sided tape.
637 Fluorescent condensation was imaged using the Nikon inverted fluorescent microscope
638 (see above). Images of fluorescent condensation were analyzed by running a Fiji macro
639 (https://github.com/masaktakaine/In-vitro-condensates-quantification). Briefly, the
640 macro automatically detects fluorescent condensation and quantifies its area and
641 fluorescence intensity.
642

MD simulation

The crystal structure of *E. coli* PPAT (PDB ID: 1ECC) was obtained from the Protein Data Bank and used for all MD simulations [39]. All water molecules and ions were removed before simulations. To build the parameters of ligands (NH_3, PRPP, and glutamic acid), their restrained electrostatic potential charges were calculated based on gas-phase HF/6-31(d) quantum mechanics calculations using Gaussian 16. A set of parameters were generated with a general AMBER force field using the antechamber from AMBER tools [51].

The Amber 14SB force field was employed for all MD simulations [52]. Missing hydrogen atoms were added by LEaP from AMBER tools. Proteins were solvated with the TIP3P water box [53]. The system was neutralized by replacing water with Na^+ or Cl^- ions. The particle-mesh Ewald (PME) method was employed for the Coulomb interaction [54]. Amber-formatted input files were converted for GROMACS using acpype [55]. All MD simulations were performed using GROMACS 2019.6 [56]. Before the production run, three-step equilibrations were performed for each system. Energy minimization was performed until 10,000 steps. This was followed by 100-ps *NVT* equilibration with the V-rescale thermostat [57] at 300 K under 1 atm. A 100-ps *NPT* equilibration was then conducted with Berendsen coupling [58] at 300 K under 1 atm. A run was performed under the *NPT* condition. The time step of each simulation was 2 fs with the SHAKE [59] and SETTLE [60] algorithms, and the snapshot was recorded every 100 ps during the production run. To examine the results of MD simulations, a Python library MDanalysis was used [61].

Data analysis

Numerical data were plotted using R studio software (R ver. 4.2.0) [62]. Means, SDs, and *p* values were calculated using Excel software (Microsoft, WA, US) and the R studio. The significance of differences between two sets of data was tested using the unpaired two-tailed Welch's *t*-test unless otherwise noted and was indicated by an asterisk or *p* value. The horizontal bar in the dot plot indicates the average of each population. All measurements were repeated at least twice to confirm reproducibility.

Acknowledgments

The authors thank the IMCR-JURSC in Gunma University for sharing research equipment. This work was supported by research grants from the Gout and Uric Acid Foundation of Japan and by JSPS KAKENHI Grant Number JP22K06216 to M.T. This study used the computational resources of Cygnus provided by the Multidisciplinary Cooperative Research Program at the Center for Computational Sciences (Project Code: MOLBIO), University of Tsukuba.

Author Contributions

MT conceived and supervised the study, MT and RM designed the experiments, MT performed the experiments, RM performed MD simulations, MT and RM analyzed the data, MT wrote the manuscript draft with input from RM, and MT and RM revised the manuscript.

Declaration of Interests

The authors declare no competing interests.

691 **References**

692 1. Yamaoka, T. *et al.* Amidophosphoribosyltransferase Limits the Rate of Cell Growth-linked de
693 Novo Purine Biosynthesis in the Presence of Constant Capacity of Salvage Purine Biosynthesis.
694 *Journal of Biological Chemistry* **272**, 17719-17725 (1997).
695 2. Daignan-Fornier, B. & Pinson, B. Yeast to Study Human Purine Metabolism Diseases. *Cells* **8**
696 (2019).
697 3. Pareek, V., Pedley, A.M. & Benkovic, S.J. Human de novo purine biosynthesis. *Crit Rev Biochem*
698 *Mol Biol*, 1-16 (2020).
699 4. Smith, J.L. *et al.* Structure of the allosteric regulatory enzyme of purine biosynthesis. *Science* **264**,
700 1427-1433 (1994).
701 5. Messenger, L.J. & Zalkin, H. Glutamine phosphoribosylpyrophosphate amidotransferase from
702 Escherichia coli. Purification and properties. *J Biol Chem* **254**, 3382-3392 (1979).
703 6. Meyer, E. & Switzer, R.L. Regulation of Bacillus subtilis glutamine phosphoribosylpyrophosphate
704 amidotransferase activity by end products. *J Biol Chem* **254**, 5397-5402 (1979).
705 7. Yamaoka, T. *et al.* Feedback inhibition of amidophosphoribosyltransferase regulates the rate of
706 cell growth via purine nucleotide, DNA, and protein syntheses. *J Biol Chem* **276**, 21285-21291
707 (2001).
708 8. Mantsala, P. & Zalkin, H. Glutamine nucleotide sequence of Saccharomyces cerevisiae ADE4
709 encoding phosphoribosylpyrophosphate amidotransferase. *J Biol Chem* **259**, 8478-8484 (1984).
710 9. Jimenez, A., Santos, M.A., Pompejus, M. & Revuelta, J.L. Metabolic engineering of the purine
711 pathway for riboflavin production in Ashbya gossypii. *Appl Environ Microbiol* **71**, 5743-5751
712 (2005).
713 10. Park, J.O. *et al.* Metabolite concentrations, fluxes and free energies imply efficient enzyme usage.
714 *Nat Chem Biol* **12**, 482-489 (2016).
715 11. Prouteau, M. & Loewith, R. Regulation of Cellular Metabolism through Phase Separation of
716 Enzymes. *Biomolecules* **8** (2018).
717 12. Cereghetti, G. *et al.* Reversible amyloids of pyruvate kinase couple cell metabolism and stress
718 granule disassembly. *Nat Cell Biol* **23**, 1085-1094 (2021).
719 13. Saad, S. *et al.* Reversible protein aggregation is a protective mechanism to ensure cell cycle restart
720 after stress. *Nature Cell Biology* **19**, 1202 (2017).
721 14. Noree, C., Monfort, E., Shiau, A.K. & Wilhelm, J.E. Common regulatory control of CTP synthase
722 enzyme activity and filament formation. *Molecular Biology of the Cell* **25**, 2282-2290 (2014).
723 15. Azzam, G. & Liu, J.L. Only one isoform of Drosophila melanogaster CTP synthase forms the
724 cytoophidium. *PLoS Genet* **9**, e1003256 (2013).
725 16. Chen, K. *et al.* Glutamine analogs promote cytoophidium assembly in human and Drosophila cells.
726 *J Genet Genomics* **38**, 391-402 (2011).

727 17. Ingerson-Mahar, M., Briegel, A., Werner, J.N., Jensen, G.J. & Gitai, Z. The metabolic enzyme
728 CTP synthase forms cytoskeletal filaments. *Nat Cell Biol* **12**, 739-746 (2010).
729 18. Lynch, E.M. *et al.* Human CTP synthase filament structure reveals the active enzyme conformation.
730 *Nat Struct Mol Biol* **24**, 507-514 (2017).
731 19. Habrian, C. *et al.* Inhibition of Escherichia coli CTP Synthetase by NADH and Other
732 Nicotinamides and Their Mutual Interactions with CTP and GTP. *Biochemistry* **55**, 5554-5565
733 (2016).
734 20. Narayanaswamy, R. *et al.* Widespread reorganization of metabolic enzymes into reversible
735 assemblies upon nutrient starvation. *Proc Natl Acad Sci U S A* **106**, 10147-10152 (2009).
736 21. An, S., Kumar, R., Sheets, E.D. & Benkovic, S.J. Reversible compartmentalization of de novo
737 purine biosynthetic complexes in living cells. *Science* **320**, 103-106 (2008).
738 22. Noree, C. *et al.* A quantitative screen for metabolic enzyme structures reveals patterns of assembly
739 across the yeast metabolic network. *Mol Biol Cell* **30**, 2721-2736 (2019).
740 23. Zacharias, D.A., Violin, J.D., Newton, A.C. & Tsien, R.Y. Partitioning of lipid-modified
741 monomeric GFPs into membrane microdomains of live cells. *Science* **296**, 913-916 (2002).
742 24. Kroschwald, S., Maharana, S. & Simon, A. Hexanediol: a chemical probe to investigate the
743 material properties of membrane-less compartments. *Matters* (2017).
744 25. Uversky, V.N. Intrinsically disordered proteins in overcrowded milieu: Membrane-less organelles,
745 phase separation, and intrinsic disorder. *Curr Opin Struct Biol* **44**, 18-30 (2017).
746 26. Jones, D.T. & Cozzetto, D. DISOPRED3: precise disordered region predictions with annotated
747 protein-binding activity. *Bioinformatics* **31**, 857-863 (2015).
748 27. Delarue, M. *et al.* mTORC1 Controls Phase Separation and the Biophysical Properties of the
749 Cytoplasm by Tuning Crowding. *Cell* **174**, 338-349.e320 (2018).
750 28. Heitman, J., Movva, N.R. & Hall, M.N. Targets for cell cycle arrest by the immunosuppressant
751 rapamycin in yeast. *Science* **253**, 905-909 (1991).
752 29. Lempiainen, H. *et al.* Sfp1 interaction with TORC1 and Mrs6 reveals feedback regulation on TOR
753 signaling. *Mol Cell* **33**, 704-716 (2009).
754 30. Fingerman, I., Nagaraj, V., Norris, D. & Vershon, A.K. Sfp1 plays a key role in yeast ribosome
755 biogenesis. *Eukaryot Cell* **2**, 1061-1068 (2003).
756 31. Pertschy, B. *et al.* Diazaborine Treatment of Yeast Cells Inhibits Maturation of the 60S Ribosomal
757 Subunit. *Molecular and Cellular Biology* **24**, 6476-6487 (2004).
758 32. Ferreira, T., Brethes, D., Pinson, B., Napias, C. & Chevallier, J. Functional analysis of mutated
759 purine-cytosine permease from Saccharomyces cerevisiae. A possible role of the hydrophilic
760 segment 371-377 in the active carrier conformation. *J Biol Chem* **272**, 9697-9702 (1997).
761 33. Jayaram, H.N. *et al.* Metabolites of alanosine, an antitumor antibiotic. *Biochem Pharmacol* **28**,
762 3551-3566 (1979).

763 34. Zhou, G., Smith, J.L. & Zalkin, H. Binding of purine nucleotides to two regulatory sites results in
764 synergistic feedback inhibition of glutamine 5-phosphoribosylpyrophosphate amidotransferase. *J*
765 *Biol Chem* **269**, 6784-6789 (1994).
766 35. Chen, S. *et al.* Mechanism of the synergistic end-product regulation of Bacillus subtilis glutamine
767 phosphoribosylpyrophosphate amidotransferase by nucleotides. *Biochemistry* **36**, 10718-10726
768 (1997).
769 36. Rebora, K., Desmoucelles, C., Borne, F., Pinson, B. & Daignan-Fornier, B. Yeast AMP pathway
770 genes respond to adenine through regulated synthesis of a metabolic intermediate. *Mol Cell Biol*
771 **21**, 7901-7912 (2001).
772 37. Mantsala, P. & Zalkin, H. Glutamine amidotransferase function. Replacement of the active-site
773 cysteine in glutamine phosphoribosylpyrophosphate amidotransferase by site-directed
774 mutagenesis. *J Biol Chem* **259**, 14230-14236 (1984).
775 38. Mei, B. & Zalkin, H. A cysteine-histidine-aspartate catalytic triad is involved in glutamine amide
776 transfer function in purF-type glutamine amidotransferases. *Journal of Biological Chemistry* **264**,
777 16613-16619 (1989).
778 39. Krahn, J.M. *et al.* Coupled formation of an amidotransferase interdomain ammonia channel and a
779 phosphoribosyltransferase active site. *Biochemistry* **36**, 11061-11068 (1997).
780 40. Holmes, E.W., McDonald, J.A., McCord, J.M., Wyngaarden, J.B. & Kelley, W.N. Human
781 glutamine phosphoribosylpyrophosphate amidotransferase. Kinetic and regulatory properties. *J*
782 *Biol Chem* **248**, 144-150 (1973).
783 41. Satyanarayana, T. & Kaplan, J.G. Regulation of the purine pathway in bakers yeast: activity and
784 feedback inhibition of phosphoribosyl-pyrophosphate amidotransferase. *Arch Biochem Biophys*
785 **142**, 40-47 (1971).
786 42. Castellana, M. *et al.* Enzyme clustering accelerates processing of intermediates through metabolic
787 channeling. *Nature Biotechnology* **32**, 1011-+ (2014).
788 43. Rodwell, V.W., Bender, D., Botham, K.M., Kennelly, P.J. & Weil, P.A. *Harpers Illustrated*
789 *Biochemistry 30th Edition*. (McGraw Hill LLC, 2015).
790 44. Takahara, T., Amemiya, Y., Sugiyama, R., Maki, M. & Shibata, H. Amino acid-dependent control
791 of mTORC1 signaling: a variety of regulatory modes. *Journal of Biomedical Science* **27**, 87 (2020).
792 45. Ben-Sahra, I., Hoxhaj, G., Ricoult, S.J.H., Asara, J.M. & Manning, B.D. mTORC1 induces purine
793 synthesis through control of the mitochondrial tetrahydrofolate cycle. *Science* **351**, 728-733 (2016).
794 46. Hunkeler, M. *et al.* Structural basis for regulation of human acetyl-CoA carboxylase. *Nature* **558**,
795 470-474 (2018).
796 47. Janke, C. *et al.* A versatile toolbox for PCR-based tagging of yeast genes: new fluorescent proteins,
797 more markers and promoter substitution cassettes. *Yeast* **21**, 947-962 (2004).
798 48. Hanscho, M. *et al.* Nutritional requirements of the BY series of Saccharomyces cerevisiae strains

for optimum growth. *FEMS Yeast Res* **12**, 796-808 (2012).

49. Schindelin, J. *et al.* Fiji: an open-source platform for biological-image analysis. *Nat Methods* **9**, 676-682 (2012).

50. von der Haar, T. Optimized protein extraction for quantitative proteomics of yeasts. *PLoS One* **2**, e1078 (2007).

51. D.A. Case, H.M.A., K. Belfon, I.Y. Ben-Shalom, J.T. Berryman, S.R. Brozell, D.S. Cerutti, T.E. Cheatham, III, G.A. Cisneros, V.W.D. Cruzeiro, T.A. Darden, R.E. Duke, G. Giambasu, M.K. Gilson, H. Gohlke, A.W. Goetz, R. Harris, S. Izadi, S.A. Izmailov, K. Kasavajhala, M.C. Kaymak, E. King, A. Kovalenko, T. Kurtzman, T.S. Lee, S. LeGrand, P. Li, C. Lin, J. Liu, T. Luchko, R. Luo, M. Machado, V. Man, M. Manathunga, K.M. Merz, Y. Miao, O. Mikhailovskii, G. Monard, H. Nguyen, K.A. O'Hearn, A. Onufriev, F. Pan, S. Pantano, R. Qi, A. Rahnamoun, D.R. Roe, A. Roitberg, C. Sagui, S. Schott-Verdugo, A. Shajan, J. Shen, C.L. Simmerling, N.R. Skrynnikov, J. Smith, J. Swails, R.C. Walker, J Wang, J. Wang, H. Wei, R.M. Wolf, X. Wu, Y. Xiong, Y. Xue, D.M. York, S. Zhao, and P.A. Kollman (University of California, San Francisco.; 2022).

52. Maier, J.A. *et al.* ff14SB: Improving the Accuracy of Protein Side Chain and Backbone Parameters from ff99SB. *J Chem Theory Comput* **11**, 3696-3713 (2015).

53. Kiss, P.T. & Baranyai, A. Sources of the deficiencies in the popular SPC/E and TIP3P models of water. *The Journal of Chemical Physics* **134**, 054106 (2011).

54. Pippig, M. & Mercuri, F. Efficient evaluation of Coulomb interactions in kinetic Monte Carlo simulations of charge transport. *The Journal of Chemical Physics* **152**, 164102 (2020).

55. Sousa da Silva, A.W. & Vranken, W.F. ACPYPE - AnteChamber PYthon Parser interfacE. *BMC Res Notes* **5**, 367 (2012).

56. M.J. Abraham, D.v.d.S., E. Lindahl, B. Hess, and the GROMACS development team (2019).

57. Bussi, G., Donadio, D. & Parrinello, M. Canonical sampling through velocity rescaling. *J Chem Phys* **126**, 014101 (2007).

58. Berendsen, H.J.C., Postma, J.P.M., van Gunsteren, W.F., DiNola, A. & Haak, J.R. Molecular dynamics with coupling to an external bath. *The Journal of Chemical Physics* **81**, 3684-3690 (1984).

59. Ryckaert, J.-P., Ciccotti, G. & Berendsen, H.J.C. Numerical integration of the cartesian equations of motion of a system with constraints: molecular dynamics of n-alkanes. *Journal of Computational Physics* **23**, 327-341 (1977).

60. Miyamoto, S. & Kollman, P.A. Settle: An analytical version of the SHAKE and RATTLE algorithm for rigid water models. *Journal of Computational Chemistry* **13**, 952-962 (1992).

61. Michaud-Agrawal, N., Denning, E.J., Woolf, T.B. & Beckstein, O. MDAnalysis: A toolkit for the analysis of molecular dynamics simulations. *Journal of Computational Chemistry* **32**, 2319-2327 (2011).

835 62. R Core Team (R Foundation for Statistical Computing, Vienna, Austria; 2017).
836 63. Chen, S., Burgner, J.W., Krahn, J.M., Smith, J.L. & Zalkin, H. Tryptophan fluorescence monitors
837 multiple conformational changes required for glutamine phosphoribosylpyrophosphate
838 amidotransferase interdomain signaling and catalysis. *Biochemistry* **38**, 11659-11669 (1999).
839

840 **Figure Legends**

841 **Figure 1. The yeast PPAT Ade4 concentrates in fine granules**

842 A. Bright field and GFP images of cells expressing Ade4 tagged C-terminally with the
843 indicated green fluorescent protein. Cells were grown in medium containing 0.02 mg/ml
844 adenine, washed with medium lacking adenine, and then incubated in medium without
845 adenine for 30 min before imaging. The intensity of GFP is represented by pseudo-colors
846 in the upper panels.

847 B. Quantification of the mean fluorescence intensity of Ade4 condensates observed in
848 cells as shown in (A). Data are represented by box and dot plots. Cross marks indicate
849 the population mean. *P* values versus mGFP are shown (Steel's multiple comparison test).

850 C. A higher resolution image of Ade4-mNG granules. Granules were imaged at an *xy*
851 resolution of 34 pixels/µm and z-spacing of 0.5 µm. Z-positions are represented by a color
852 code (left). A grayscale image of granules (middle) and bright field image of cells (right)
853 are also shown. Scale bar = 5 µm.

854 D. Time-lapse imaging of the assembly of Ade4-mNG granules by adenine depletion.
855 Cells were grown in medium containing 0.02 mg/ml adenine and washed with medium
856 lacking adenine at t = 0 min. Scale bar = 5 µm.

857 E. Time-lapse imaging of the disassembly of Ade4-mNG granules by adenine
858 supplementation. Cells were grown in the absence of adenine and 0.02 mg/ml adenine
859 was supplemented at t = 0 min. Scale bar = 5 µm.

860 F, G. Panels F and G show the quantification of data in (D) and (E), respectively. The
861 number of intracellular Ade4-mNG granules was counted as the number of maxima of
862 green fluorescence intensity per cell. Data are the mean over 10-12 independent fields of
863 view, and approximately 70 cells were examined per field. The shaded area indicates ±
864 1SD.

865 H. Schematic of *de novo* purine synthesis

866

867 **Figure 1S1. Additional data regarding the intracellular localization of Ade4. Related**
868 **to Figure 1**

869 A. Bright field and GFP images of cells expressing Ade4 tagged C-terminally with the
870 indicated green fluorescent protein. Cells were grown in medium containing 0.02 mg/ml
871 adenine and imaged.

872 B. Phase and RFP images of cells expressing Ade4 tagged C-terminally with the red
873 fluorescent protein mKate2. Scale bar = 5 µm.

874 C. A control experiment of time-lapse imaging of the assembly of Ade4-mNG granules
875 by adenine depletion shown in Fig. 1D. Cells were grown in medium containing 0.02

876 mg/ml adenine and washed with medium containing the same concentration of adenine
877 at t = 0 min. Scale bar = 5 μm.
878 D. A control experiment of time-lapse imaging of the disassembly of Ade4-mNG granules
879 by adenine supplementation shown in Fig. 1E. Cells were grown in the absence of adenine
880 and sterile water was supplemented in place of adenine at t = 0 min. Scale bar = 5 μm.
881
882 **Figure 2. Ade4 granules have liquid-like properties**
883 A. The aliphatic alcohol 1,6–hexanediol dissolves Ade4 granules. Cells harboring Ade4-
884 mNG granules in the absence of purine bases were treated with 2 μg/ml digitonin ± 10%
885 (w/v) 1,6-hexanediol for 10 min and then imaged. Scale bar = 5 μm.
886 B. Quantification of data shown in (A). The percentage of cells with Ade4-mNG granules
887 per field of view (containing 361 ± 159 cells) was plotted. Data were pooled from three
888 independent experiments. Bars and error bars indicate the mean ± 1SD. *P* values were
889 calculated using the two-tailed Steel-Dwass multiple comparison test.
890 C. Domain structure of the budding yeast Ade4. The bottom graph shows disorder
891 predictions by the DISOPRED algorithm.
892 D. The C-terminal IDR of Ade4 is required for granule assembly. Cells expressing the
893 mutant Ade4 lacking the C-terminal IDR tagged with mNG were incubated in the absence
894 of purine bases for 40 min and imaged.
895
896 **Figure 2S1. The C-terminal IDR is conserved in PPATs of Ascomycota**
897 Heatmap showing the disorder scores of PPAT amino acid sequences of 81 ascomycota.
898
899 **Figure 2S2. The IDR is conserved in PPATs of various species**
900 Heatmap showing the disorder scores of PPAT amino acid sequences of 100 organisms,
901 including 19 ascomycota. Phylogenetic groups are color-coded on the left.
902
903 **Figure 2S3. Amino acid sequences of IDRs vary across species**
904 A-B. Multiple amino acid sequence alignment of the C-terminal region of PPAT. In (A),
905 three fungi and 13 representative organisms from the following groups are selected:
906 archaea, bacteria, protozoa, plants, nematodes, insects, echinoidea, fish, amphibians,
907 mammals, reptiles, birds, and ascidians. In (B), 13 species are selected from ascomycota.
908
909 **Figure 3. Formation of Ade4 granules requires active TORC1 and ribosome**
910 **biogenesis**
911 A. Wild-type and *fpr1*Δ cells expressing Ade4-GFP were grown in medium containing

912 adenine and incubated in medium without adenine in the presence of 0.02% (v/v) DMSO
913 or 0.02% DMSO plus 2 μg/ml rapamycin for 30 min before imaging.
914 B. Rapamycin suppresses the assembly of Ade4-mNG granules. Wild-type cells
915 expressing Ade4-mNG were treated with rapamycin and imaged as described in (A).
916 C. Quantification of data shown in (B). The percentage of cells with Ade4-mNG granules
917 per field of view (containing 443 ± 138 cells) was plotted. Data were pooled from two
918 independent experiments. Bars and error bars indicate the mean ± 1SD. *P* values were
919 calculated using the two-tailed Mann-Whitney U test.
920 D. The assembly of Ade4-mNG granules was significantly suppressed in *sfp1*Δ and *sit4*Δ
921 cells.
922 E. Quantification of data shown in (C). The percentage of cells with Ade4-mNG granules
923 per field of view (containing 517 ± 123 cells) was plotted. Data were pooled from three
924 independent experiments. Bars and error bars indicate the mean ± 1SD. *P* values versus
925 wt were calculated using the two-tailed Steel's multiple comparison test.
926 F. The inhibition of ribosome synthesis suppresses the assembly of Ade4 condensates.
927 Cells expressing Ade4-GFP were grown in medium containing adenine and then
928 incubated in medium without adenine in the presence of 0.05% (v/v) DMSO or 0.05%
929 DMSO plus 5 μg/ml diazaborine for 30 min before imaging. The percentage of cells with
930 Ade4-GFP foci per field of view (containing 780 ± 214 cells) was plotted. Data were
931 pooled from two independent experiments. Bars and error bars indicate the mean ± 1SD.
932 *P* values were calculated using the two-tailed Mann-Whitney U test. Representative cell
933 images are shown in Figure 3S1C. Scale bar = 5 μm.
934
935 **Figure 3S1. Formation of Ade4 granules in TORC1-related mutants. Related to**
936 **Figure 3.**
937 A. Assembly of Ade4-GFP foci in single gene deletion mutants of the upstream regulator
938 and downstream effector of TORC1 signaling. Cells of the indicated genotype expressing
939 Ade4-GFP were grown in medium containing adenine and then incubated in medium
940 without adenine for 30 min before imaging.
941 B. Summary of the percentage of cells showing Ade4-GFP foci in the wild-type and 37
942 single-gene deletion mutants. The percentage of cells with Ade4-GFP foci per field of
943 view was plotted. Data were pooled from 2-3 independent experiments. Bars and error
944 bars indicate the mean ± 1SD.
945 C. The inhibition of ribosome synthesis suppressed the assembly of Ade4-GFP foci.
946 Related to Figure 3F.
947 D. The inhibition of ribosome synthesis suppressed the assembly of Ade4-mNG granules.

948 Cells expressing Ade4-mNG were grown in medium containing adenine and then
949 incubated in medium without adenine in the presence of 0.05% (v/v) DMSO or 0.05%
950 DMSO plus 5 μg/ml diazaborine for 30 min before imaging. Scale bar = 5 μm.
951
952 **Figure 4. Intracellular derivatives of purine nucleotides prevent the formation of**
953 **Ade4 condensates**
954 A. *De novo* and salvage pathways for purine synthesis in budding yeast.
955 B. Assembly of Ade4-GFP foci in purine metabolism mutants. Cells having Ade4-GFP
956 foci in the absence of purine bases (mock) were treated with the same medium or medium
957 containing 20 μg/adenine (+adenine) or 25 μg/ml hypoxanthine (+hypoxanthine) for 20
958 min and then imaged. Scale bar = 5 μm.
959 C-E. Quantification of data shown in (B). The percentage of cells with foci per field of
960 view was quantified and plotted. Bars and error bars indicate the mean ± 1SD. Data were
961 pooled from 2-3 independent experiments, and more than 16 fields of view were imaged
962 for each condition. Triple asterisks indicate *p* values less than 10^{-10} versus the mock
963 (Steel's multiple comparison test, two-tailed). The single asterisk indicates a *p* value less
964 than 0.01 versus the mock. NS, not significant (*p* value >0.05).
965
966 **Figure 4S1. Alanosine inhibits the dissolution of Ade4 foci in the presence of**
967 **hypoxanthine. Related to Figure 4.**
968 A. Alanosine inhibits the adenylosuccinate synthetase ADE12.
969 B. Assembly of Ade4-GFP foci in the presence of alanosine. Cells expressing Ade4-GFP
970 were incubated in medium lacking adenine in the presence of 0 (mock) or 30 μg/ml
971 alanosine (+alanosine) for 40 min to allow the assembly of Ade4-GFP foci and were then
972 imaged (SC). Cells were further treated with the same medium supplemented with 24
973 μg/ml hypoxanthine for 15 min and then imaged again (SC + hyp). Scale bar = 5 μm.
974 C. Quantification of data shown in (B). The percentage of cells with foci per field of view
975 (containing 182 ± 46 cells) was quantified and plotted. Data were pooled from two
976 independent experiments. Bars and error bars indicate the mean ± 1SD. The significance
977 of differences was tested using the unpaired one-tailed Welch's *t*-test. *P* values versus the
978 mock are shown.
979
980 **Figure 5. The interaction of purine nucleotides with Ade4 is implicated in granule**
981 **assembly**
982 A. Interaction between ADP and specific amino acid residues in *B. subtilis* PPAT (pdb
983 file: 1ao0). The dotted line indicates a hydrogen bond.

984 B. Amino acid residues involved in the interaction with purine nucleotides are well
985 conserved among species.
986 C-E. Examination of the Ade4-VQQ mutant. Ade4-mNG and Ade4-VQQ-mNG cells
987 were incubated in medium without purine bases for 40 min to allow for the assembly of
988 Ade4 granules and then imaged. The percentage of cells with granules per field of view
989 (containing 265 ± 80 cells) was quantified and plotted in (C). The number of granules
990 detected in the cell were averaged over the field of view and plotted in (D). The mean
991 fluorescence intensity of granules was box plotted in (E). Data were pooled from three
992 independent experiments. Bars and error bars indicate the mean ± 1SD. The significance
993 of differences was tested using the unpaired two-tailed Welch's *t*-test (C) or Mann-
994 Whitney U test (D, E). *P* values versus wt are shown.
995
996 **Figure 6. The Ade4 protein condensates into particles under molecular crowding**
997 **conditions *in vitro***
998 A. Pure Ade4-mNG condensated into fine particles in a PEG concentration-dependent
999 manner. Following the supplementation of 0.15 μM Ade4-mNG with PEG8000 at the
1000 indicated concentration (%, w/v), images were taken after a 1-min incubation. Inverted
1001 grayscale images are shown. Scale bar = 5 μm.
1002 B-C. Quantification of data shown in (A). The mean fluorescence intensities of Ade4-
1003 mNG particles were box plotted in (B). Cross marks indicate the population mean. The
1004 integrated fluorescence intensities of particles were summed per field and plotted in (C).
1005 Bars and error bars indicate the mean ± 1SD. Seven to 10 fields of view were imaged for
1006 each condition and an average of 390 particles per field were examined.
1007 D. 1,6-Hexanediol attenuated the *in vitro* condensation of Ade4-mNG. Following the
1008 supplementation of 0.15 μM Ade4-mNG with 10% PEG8000 in the presence of 0 or 10%
1009 (w/v) 1,6-hexanediol, images were taken after a 1-min incubation. Fluorescence intensity
1010 is represented by pseudo-colors. Scale bar = 5 μm.
1011 E-F. Quantification of data shown in (D). The mean fluorescence intensities of particles
1012 were box plotted in (E). Cross marks indicate the population mean. The integrated
1013 fluorescence intensities of particles were summed per field and plotted in (F). Bars and
1014 error bars indicate the mean ± 1SD. Ten fields of view were imaged for each condition,
1015 and an average of 1197 particles per field were examined. *P* values were calculated using
1016 the two-tailed Mann-Whitney U test (E) or Welch's *t*-test (F).
1017 G. Ade4ΔIDR-mNG assembled into granules less effectively than Ade4-mNG *in vitro*.
1018 Following the supplementation of 0.2 μM Ade4-mNG or Ade4ΔIDR-mNG with 10%
1019 PEG8000, images were taken after a 1-min incubation. Fluorescence intensity is

represented by pseudo-colors. Scale bar = 5 μm.

H-I. Quantification of data shown in (G). The mean fluorescence intensities of particles were box plotted in (H). Cross marks indicate the population mean. The integrated fluorescence intensities of particles were summed per field and plotted in (I). Bars and error bars indicate the mean ± 1SD. Twenty-eight fields of view were imaged for each condition, and an average of 1341 particles per field were examined. *P* values were calculated using the two-tailed Mann-Whitney U test.

Figure 6S1. Purification and basic characterization of the Ade4 protein *in vitro*

A. Purified proteins used in the present study. Proteins were resolved by SDS-PAGE and stained with FastGene™ Q-stain.

B. The pure mNG protein did not condensate into particles even under molecular crowding conditions. Following the supplementation of 0.14 μM mNG with 0 or 10% PEG8000, images were taken after a 1-min incubation. Scale bar = 5 μm.

C. The *in vitro* condensation of Ade4-mNG depends on the size of PEG. Following the supplementation of 0.15 μM Ade4-mNG with 10% PEG of the indicated average molecular weight, images were taken after a 1-min incubation. Scale bar = 5 μm.

D-E. Quantification of data shown in (C). The mean fluorescence intensities of Ade4-mNG particles were box plotted in (D). Cross marks indicate the population mean. The integrated fluorescence intensities of particles were summed per field and plotted in (E). Bars and error bars indicate the mean ± 1SD. Seven to 8 fields of view were imaged for each condition, and an average of 399 particles per field were examined.

F. Condensation of Ade4-mNG into particles with crowding agents other than PEG. Between 0.13 and 0.14 μM Ade4-mNG was supplemented with the indicated crowding agents and images were taken after a 1-min incubation. Scale bar = 5 μm.

Figure 6S2. Estimation of the intracellular concentration of Ade4.

Data regarding the protein abundance of the budding yeast Ade4 were downloaded from the Saccharomyces Genome Database (https://www.yeastgenome.org/locus/S000004915/protein). Data were derived from twenty quantitative genome-wide proteomic studies and normalized to a unit of molecules per cell. These values were converted to micromoles assuming that the average cytoplasmic volume of the haploid yeast cell is 42 fℓ (Jorgensen et al., 2002). Data were classified according to the condition of cells (unstressed or stressed), measuring methods (flow cytometry, quantitative fluorescence microscopy, and immunoblotting), and the type of medium (rich or synthetic) and then plotted. Bars and error bars indicate the mean

1056 ± 1SD.
1057
1058 **Figure 7. Purine nucleotides attenuate the assembly of Ade4 particles *in vitro***
1059 A. Effects of purine nucleotides on the *in vitro* assembly of Ade4 particles. Following the
1060 supplementation of 0.2 μM Ade4-mNG with 10% PEG8000 in the presence of the
1061 indicated purine nucleotide, images were taken after a 2-min incubation. The integrated
1062 fluorescence intensities of particles were summed per field and plotted. Bars and error
1063 bars indicate the mean ± 1SD. Between 23 and 28 fields of view were imaged for each
1064 condition from two independent preparations, and an average of 1323 particles per field
1065 were examined. *P* values were calculated using the two-tailed Tukey-Kramer's multiple
1066 comparison test. ***, $p < 0.001$; NS, not significant (p value > 0.05).
1067 B-D. The supplementation of 0.2 μM Ade4-mNG with 10% PEG8000 was performed in
1068 the presence of the indicated concentration of AMP (B), ADP (C), and ATP (D). The
1069 integrated fluorescence intensities of particles were summed per field, normalized to the
1070 mean at 0 μM, and plotted. Bars and error bars indicate the mean ± 1SD. Between 28 and
1071 55 fields of view were imaged for each condition from 2 or 3 independent preparations,
1072 and an average of 1200 particles per field were examined.
1073 E. Effects of AMP on the *in vitro* assembly of Ade4 and Ade4ΔIDR particles. The
1074 supplementation of 0.2 μM Ade4-mNG (FL) or Ade4ΔIDR-mNG (ΔIDR) with 10%
1075 PEG8000 was performed in the presence of 0 or 500 μM AMP. The integrated
1076 fluorescence intensities of particles were summed per field, normalized to the mean of
1077 FL at 0 μM AMP, and plotted. Bars and error bars indicate the mean ± 1SD. Between 40
1078 and 45 fields of view were imaged for each condition from 3 independent preparations.
1079 *P* values were calculated using the two-tailed Welch's *t*-test.
1080 F. Schematic model showing the regulation of Ade4 condensation proposed in the present
1081 study. See the text for details.
1082
1083 **Figure 7S1. Additional data regarding the assembly of Ade4 particles *in vitro*, related**
1084 **to Fig. 7.**
1085 A, B. Effects of purine base derivatives on the *in vitro* assembly of Ade4 particles.
1086 Following the supplementation of 0.2 μM Ade4-mNG with 10% PEG8000 in the
1087 presence of the indicated compound, images were taken after a 2-min incubation. Glucose
1088 was used as a negative control. The integrated fluorescence intensities of particles were
1089 summed per field and plotted in (A). The mean fluorescence intensities of Ade4-mNG
1090 particles were averaged per field and plotted in (B). Bars and error bars indicate the mean
1091 ± 1SD. Twenty fields of view were imaged for each condition from two independent

1092 preparations, and an average of 1452 particles per field were examined. *P* values were
1093 calculated using the two-tailed Steel's multiple comparison test. NS, not significant (*p*
1094 value >0.05).
1095 C. Effects of purine nucleotides on the *in vitro* assembly of Ade4 particles. Data were
1096 from the same experiment shown in Figure 7A. The mean fluorescence intensities of
1097 Ade4-mNG particles were averaged per field and plotted. Bars and error bars indicate the
1098 mean ± 1SD. *P* values were calculated using the two-tailed Tukey-Kramer's multiple
1099 comparison test. ***, $p < 0.001$; NS, not significant (*p* value >0.05).
1100 D. The supplementation of 0.2 μM Ade4-mNG with 10% PEG8000 was performed in the
1101 presence of the indicated concentration of GMP. The integrated fluorescence intensities
1102 of particles were summed per field, normalized to the mean at 0 μM, and plotted. Bars
1103 and error bars indicate the mean ± 1SD. Between 25 and 30 fields of view were imaged
1104 for each condition from two independent preparations, and an average of 1200 particles
1105 per field were examined.
1106
1107 **Figure 8. The formation of Ade4 granules is important for efficient *de novo* purine**
1108 **synthesis during cell growth**
1109 A. Growth of ADE4-3HA and ADE4ΔIDR-3HA cells on solid media. Cells of each strain
1110 were serially diluted (five-fold), spotted on 2% glucose medium containing the indicated
1111 nitrogen source, and then grown at 30°C for 2-3 days.
1112 B. Immunoblot analysis of the protein level of Ade4. Total cell extracts were prepared
1113 from cells expressing the indicated Ade4 construct. Ade4-3HA and Ade4ΔIDR-3HA were
1114 detected as approximately 60-kDa bands by an anti-HA antibody. The bands of GAPDH
1115 were shown as a loading control.
1116 C. Growth curves of Ade4-3HA and Ade4ΔIDR-3HA cells in liquid media without
1117 adenine. Cells were grown at 30°C for 40 h in medium containing the indicated nitrogen
1118 source in the absence of adenine. Data are the mean of 6 replicates, and the shaded area
1119 indicates ± 1SD.
1120 D. Quantification of data shown in (C). The time to half-maximum density
1121 (corresponding to normalized OD_{595} = 0.5) was calculated and plotted. Bars and error
1122 bars indicate the mean ± 1SD. *P* values were calculated using the two-tailed Welch's *t*-
1123 test.
1124
1125 **Figure 8S1. Cell growth assay in the presence of external purine bases, related to Fig.**
1126 **8.**
1127 A. Growth curves of Ade4-3HA and Ade4ΔIDR-3HA cells in liquid media containing

1128 adenine. Cells were grown at 30°C for 40 h in medium containing the indicated nitrogen
1129 source in the presence of adenine. Data are the mean of 6 replicates, and the shaded area
1130 indicates ± 1SD.
1131 B. Quantification of data shown in (A). The time to half-maximum density
1132 (corresponding to normalized OD_{595} = 0.5) was calculated and plotted. Bars and error
1133 bars indicate the mean ± 1SD. *P* values were calculated using the two-tailed Welch's *t*-
1134 test.
1135 C. Reaction formulae corresponding to the glutamine-dependent PRA synthesis (Gln-
1136 PRA activity) and NH_3-dependent PRA synthesis (NH_3-PRA activity) of PPAT.
1137 D. Relationship between ammonia concentrations and the two activities of PPAT.
1138
1139 **Figure 9. MD calculations predict the potential leakage of glutamine-derived NH_3**
1140 **from PPAT molecules**
1141 (A-C) Time series for the dihedral angle of the Phe260 side chain and the distance of NH_3
1142 from the initial structure (A: holo; B: semi-holo; and C: R333A mutant). Moving averages
1143 are plotted in bold lines. Under each condition, 100-ns simulations were performed ten
1144 times individually. The blue backgrounds indicate the open state of the Phe260 sidechain.
1145 (D) The hydrophobic (orange) and front (red) channels of *E. coli* PPAT. (E) A structural
1146 snapshot around the Arg gate. Hydrogen bonds are shown as red dotted lines. (F) The
1147 reaction mechanism suggested in a previous study. (G) The reaction mechanism
1148 suggested in the present study. (H) Intramolecular and intermolecular channeling of NH_3.
1149
1150 **Figure 9S1. Possible enzymatic reaction pathways of PPAT**
1151 A. Intramolecular channeling of glutamine-derived NH_3 proposed by Krahn et al.[39].
1152 B. Mechanism of NH_3-dependent activity proposed by Chen et al.[63]. External NH_3 enters
1153 the channel from the glutamine site irrespective of glutamine binding.
1154 C. The MD simulation in the present study suggests that glutamine-derived NH_3 leaks
1155 through the front channel following the attack of exogenous NH_3.
1156 D. Condensation-dependent activation of Ade4 proposed by the present study. Glutamine-
1157 derived NH_3 leaked from the front channel rapidly diffuses away. In the Ade4 condensate,
1158 the opportunity for NH_3 to be captured by other molecules and further reacted with PRPP
1159 will increase. This activation may be described as intermolecular NH_3 channeling. PRPP
1160 is not depicted in the schema.

1161 **Supplemental Information**

1162 Table S1. Budding yeast strains used in this study

Name	genotype	Source	Figure
MTY3509	ade4-yeGFP	This study	1, 1S1, 3, 4, 5
MTY3545	sch9Δ ade4-yeGFP	This study	3S1
MTY3546	ypk3Δ ade4-yeGFP	This study	3S1
MTY3547	rim15Δ ade4-yeGFP	This study	3S1
MTY3550	gcn2Δ ade4-yeGFP	This study	3S1
MTY3551	atg13Δ ade4-yeGFP	This study	3S1
MTY3558	mks1Δ ade4-yeGFP	This study	3S1
MTY3560	gat1Δ ade4-yeGFP	This study	3S1
MTY3562	gln3Δ ade4-yeGFP	This study	3S1
MTY3563	tco89Δ ade4-yeGFP	This study	3S1
MTY3565	fpr1Δ ade4-yeGFP	This study	3
MTY3566	sit4Δ ade4-yeGFP	This study	3S1
MTY3567	sfp1Δ ade4-yeGFP	This study	3S1
MTY3571	ade4-mNG-hphNT1	This study	1, 1S1, 2, 3, 3S1
MTY3573	rtg2Δ ade4-yeGFP	This study	3S1
MTY3579	ade4-myeGFP-hph	This study	1, 1S1
MTY3613	rts1Δ ade4-yeGFP	This study	3S1
MTY3614	npr3Δ ade4-yeGFP	This study	3S1
MTY3615	npr2Δ ade4-yeGFP	This study	3S1
MTY3616	seh1Δ ade4-yeGFP	This study	3S1
MTY3617	sea2Δ ade4-yeGFP	This study	3S1
MTY3618	sea3Δ ade4-yeGFP	This study	3S1
MTY3619	sea4Δ ade4-yeGFP	This study	3S1
MTY3620	lst4Δ ade4-yeGFP	This study	3S1
MTY3621	lst7Δ ade4-yeGFP	This study	3S1
MTY3622	gtr1Δ ade4-yeGFP	This study	3S1
MTY3623	ego1Δ ade4-yeGFP	This study	3S1
MTY3624	ego2Δ ade4-yeGFP	This study	3S1
MTY3625	ego3Δ ade4-yeGFP	This study	3S1

MTY3626	pib2Δ ade4-yeGFP	This study	3S1
MTY3633	sap4Δ ade4-yeGFP	This study	3S1
MTY3634	sap155Δ ade4-yeGFP	This study	3S1
MTY3635	sap190Δ ade4-yeGFP	This study	3S1
MTY3636	maf1Δ ade4-yeGFP	This study	3S1
MTY3637	tod6Δ ade4-yeGFP	This study	3S1
MTY3638	gcn4Δ ade4-yeGFP	This study	3S1
MTY3640	ade4-3HA-hph	This study	8, 8S1
MTY3650	hpt1Δ ade4-yeGFP	This study	4
MTY3653	ade12Δ::nat ade4-yeGFP	This study	4
MTY3685	cdc55Δ ade4-yeGFP	This study	3S1
MTY3686	kap120Δ ade4-yeGFP	This study	3S1
MTY3688	sfp1Δ ade4-mNG	This study	3
MTY3689	sit4Δ ade4-mNG	This study	3
MTY3694	ade4-yeGFP tpd3Δ::natNT2	This study	3S1
MTY3698	ade4 (1-484T)-3HA	This study	8, 8S1
MTY3700	ade4 (1-484T)-mNG	This study	2
MTY3701	Y13206 Ade4-yeGFP	This study	4S1
MTY3731	gtr2Δ::nat ade4-yeGFP	This study	3S1
MTY3762	BY4741	Lab stock	8
MTY3872	aah1Δ apt1Δ Ade4-yeGFP	This study	4
MTY3882	Ade4-mKate2	This study	1S1
MTY3920	Ade4 (D310V, K333Q, R335Q)-mNG	This study	5
MTY3944	PGPD-Ade4-mNG-Strep-tag II	This study	6, 6S1, 7, 7S1
MTY3968	PGPD-Ade4ΔIDR-mNG-Strep-tag II	This study	6, 7
MTY3969	his3Δ1::pRS303-Pgpd-mNG-Strep-tag-hphNT1 leu2Δ0 lys2Δ0 ura3Δ0	Lab stock	6S1

1163

1164

1165 Table S2. Plasmids used in this study

Name	Structure	Source	Purpose
MTP165	pFA6a-mNG-hphNT1	Lab Stock	C-terminal tagging with mNG
MTP3013	pFA6a-natNT2	Lab Stock (EUROSCARF, Janke et al., 2004)	Gene deletion by natNT2 cassette
MTP3022	pYM24	Lab Stock (EUROSCARF, Janke et al., 2004)	C-terminal tagging with 3HA
MTP3023	pYM25	Lab Stock (EUROSCARF, Janke et al., 2004)	C-terminal tagging with yeGFP
MTP3069	pYM-N15	Lab Stock (EUROSCARF, Janke et al., 2004)	Replacement of native promoter with GPD promoter
MTP3114	pYM25-A206K	This study	C-terminal tagging with monomeric yeGFP
MTP3131	pFA6a-mKate2-hphNT1	This study	C-terminal tagging with mKate2
MTP3139	pFA6a-mNG-Strep tag-hphNT1	This study	C-terminal tagging with mNG-Strep tag II

1166

1167

1168 Table S3. Primers used in this study

Name	Sequence (5' -> 3')	Purpose
ade4F1	ATCAGATATGAAGGCTGAAGTCGATATCGGATTATATAATTGTGCAGATTATCGT ACG CTG CAG GTC GAC	Ade4-GFP, Ade4-mGFP, Ade4-mNG, Ade4-mKate2, Ade4-3HA, Ade4-mNG-Strep-tag
ade4F21	CGGAAATTATGTCACTGGTGTTGAAGACGGTTATATTCAAGAATTGGAAGAAACG CTG CAG GTC GAC GGA	Ade4△IDR-mNG, Ade4△IDR-3HA, Ade4△IDR-mNG-Strep-tag
ade4F30	TAATAAGTTTAGCAAAGAAAGAGGTACAGCAAACAGCAGAATAGAAAAAATGCGTACGCTGCAGGTCGAC	Replacement of the ADE4 promoter
ade4R1	CATTTGGAAACTATTTTACATACAACTGAACAAGTTCGGAACAATCTATCAATCGATGAATTCGAGCTCG	C-terminal tagging of ADE4 locus
ade4R11	GGAGCTACTGGAGTGGTTTGGTTTGCTAATACAATACCTAAAATACCACACATCGATGAATTCTCTGTCG	Replacement of the ADE4 promoter
ade12F1	GGATAAGGTAGGGGAAATCGTAACATTACTAAATTTAAAGCATATCAGAATGCGTACGCTGCAGGTCGAC	ade12△::natNT2
ade12R1	AACTGTGAAAAGAAATTAAATTGAAGTTTGTCATGGATGTCCAACGCCCTAATCGATGAATTCGAGCTCG	ade12△::natNT2
gtr2F1	TCCACAGATTAACAAAACTCCAGGACAACGGTACTAATACACATACAACATGCGTACGCTGCAGGTCGAC	gtr2△::natNT2
gtr2R1	TTTTCAATATGTATCTATATACCCTAATATTTTCATGCCTTACGTCTTTCAATCGATGAATTCGAGCTCG	gtr2△::natNT2
tpd3F2	TGGTATCTGATTATCGAAGAATAATTGAGTGGTCAGAAAGGAGCGAAATATGCGTACGCTGCAGGTCGAC	tpd3△::natNT2
tpd3R1	TTCATTCAAGTGTACATATGTGTATGTATGTATATATTTGAACTAGTATCAATCGATGAATTCGAGCTCG	tpd3△::natNT2

1169

1170

1171 Captions for supplementary movies

1172 **Movie S1**

1173 Time-lapse imaging of the assembly of Ade4-mNG granules by adenine depletion. Cells
1174 were grown in medium containing 0.02 mg/ml adenine and washed with medium lacking
1175 adenine at t = 0 min. The three cells in the upper right are shown in Fig. 1D. Scale bar =
1176 5 µm.

1177

1178 **Movie S2**

1179 Another example of cells showing the assembly of Ade4-mNG granules by adenine
1180 depletion. Experimental conditions are the same as in Movie S1. Scale bar = 5 µm.

1181

1182 **Movie S3**

1183 A control experiment of time-lapse imaging of the assembly of Ade4-mNG granules by
1184 adenine depletion. Cells were grown in medium containing 0.02 mg/ml adenine and
1185 washed with medium containing the same concentration of adenine at t = 0 min. The
1186 rightmost cell is shown in Fig. 1S1C. Scale bar = 5 µm.

1187

1188 **Movie S4**

1189 Time-lapse imaging of the disassembly of Ade4-mNG granules by adenine
1190 supplementation. Cells were grown in the absence of adenine and 0.02 mg/ml adenine
1191 was supplemented at t = 0 min. The four cells in the upper left are shown in Fig. 1E. Scale
1192 bar = 5 µm.

1193

1194 **Movie S5**

1195 A control experiment of time-lapse imaging of the disassembly of Ade4-mNG granules
1196 by adenine supplementation. Cells were grown in the absence of adenine and sterile water
1197 was supplemented in place of adenine at t = 0 min. The two cells in the center are shown
1198 in Fig. 1S1D. Scale bar = 5 µm.

1199

1200 **Movie S6**

1201 Another example of cells showing Ade4-mNG granules after a mock treatment with
1202 adenine. Experimental conditions are the same as in Movie S5. Scale bar = 5 µm.

1203

Figure 1: The yeast PPAT Ade4 concentrates in fine granules

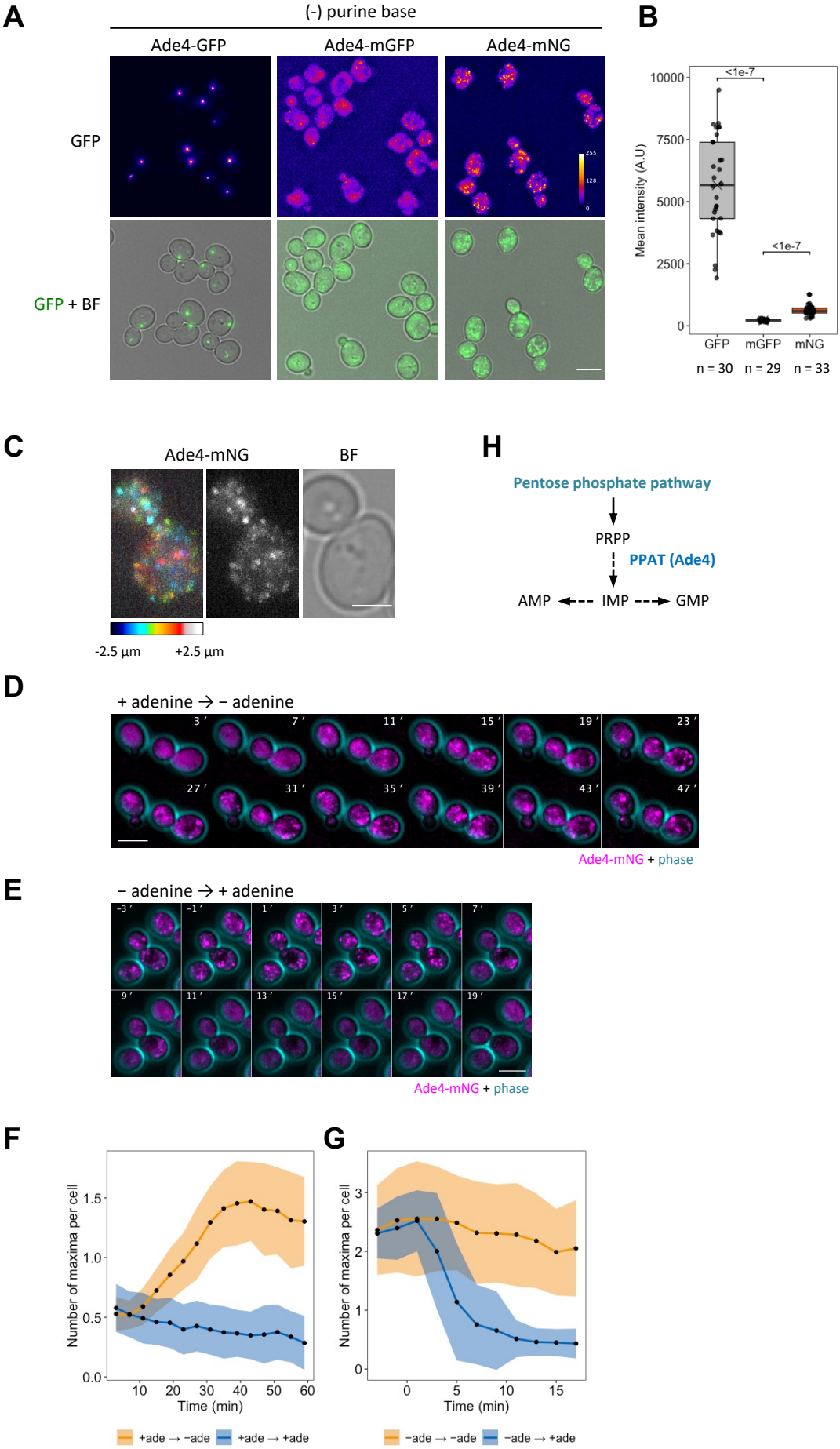

Figure 1S1: Additional data regarding the intracellular localization of Ade4. Related to Figure 1

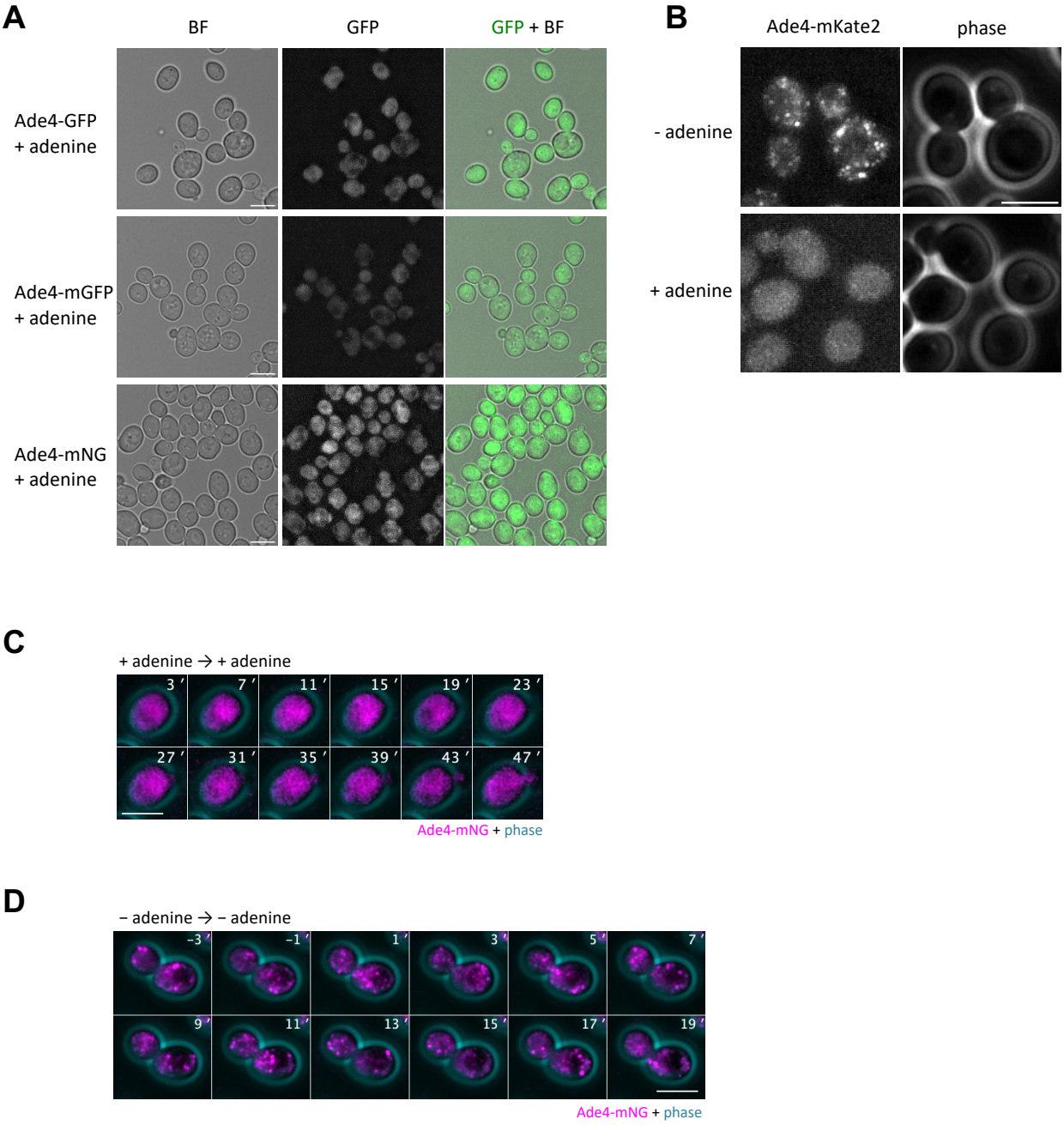

Figure 2: Ade4 granules have liquid-like properties

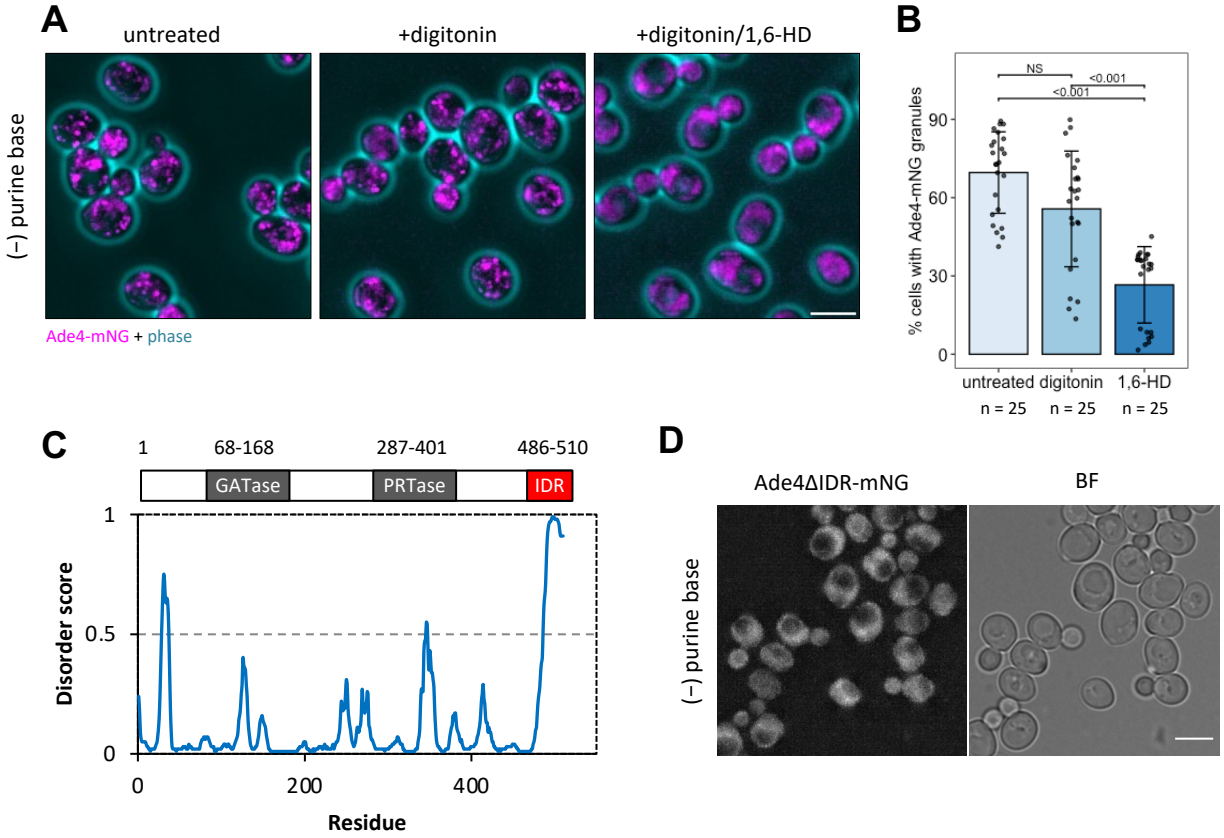

Figure 2S1: The C-terminal IDR is conserved in PPATs of Ascomycota

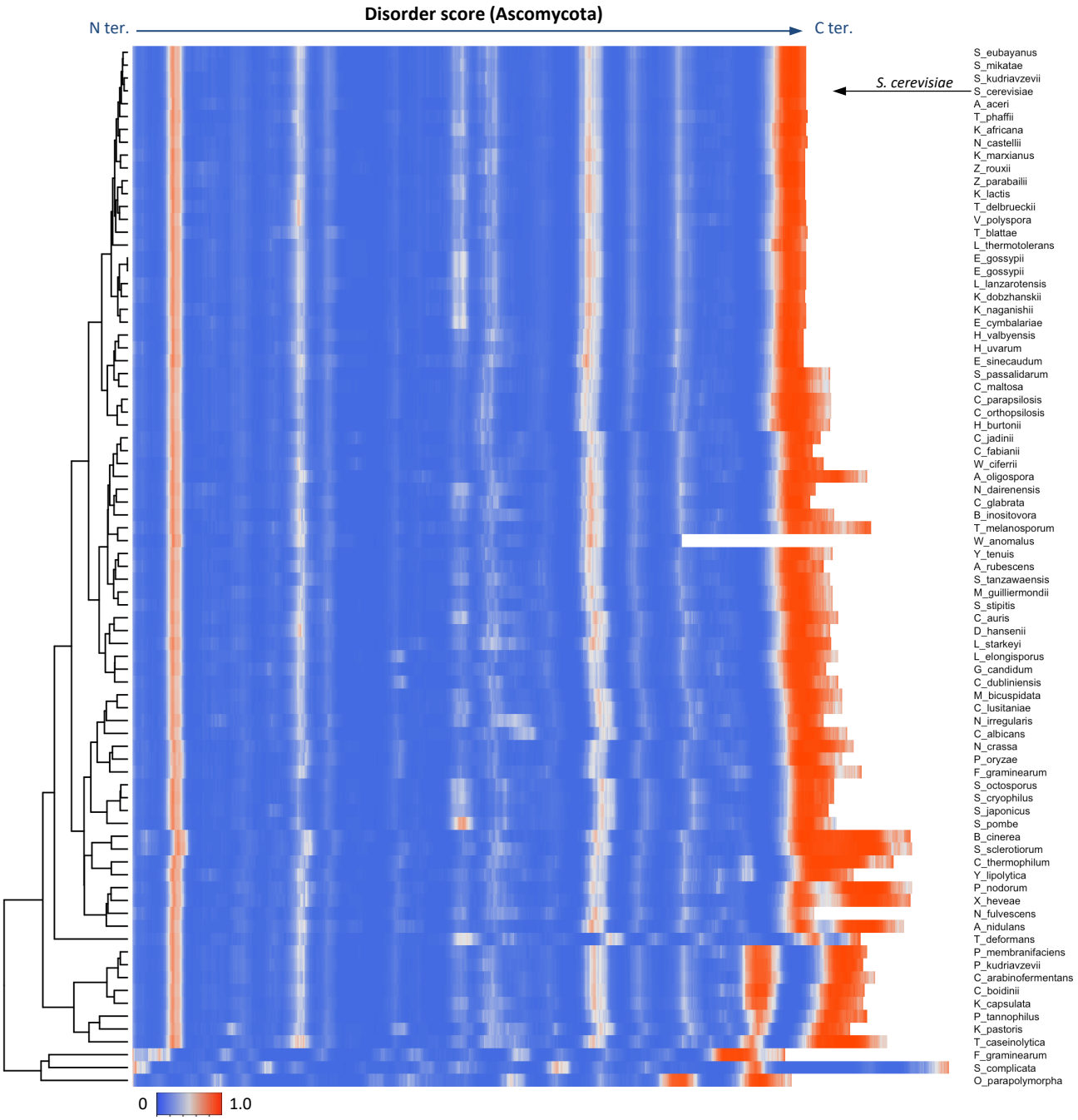

Figure 2S2: The IDR is conserved in PPATs of various species

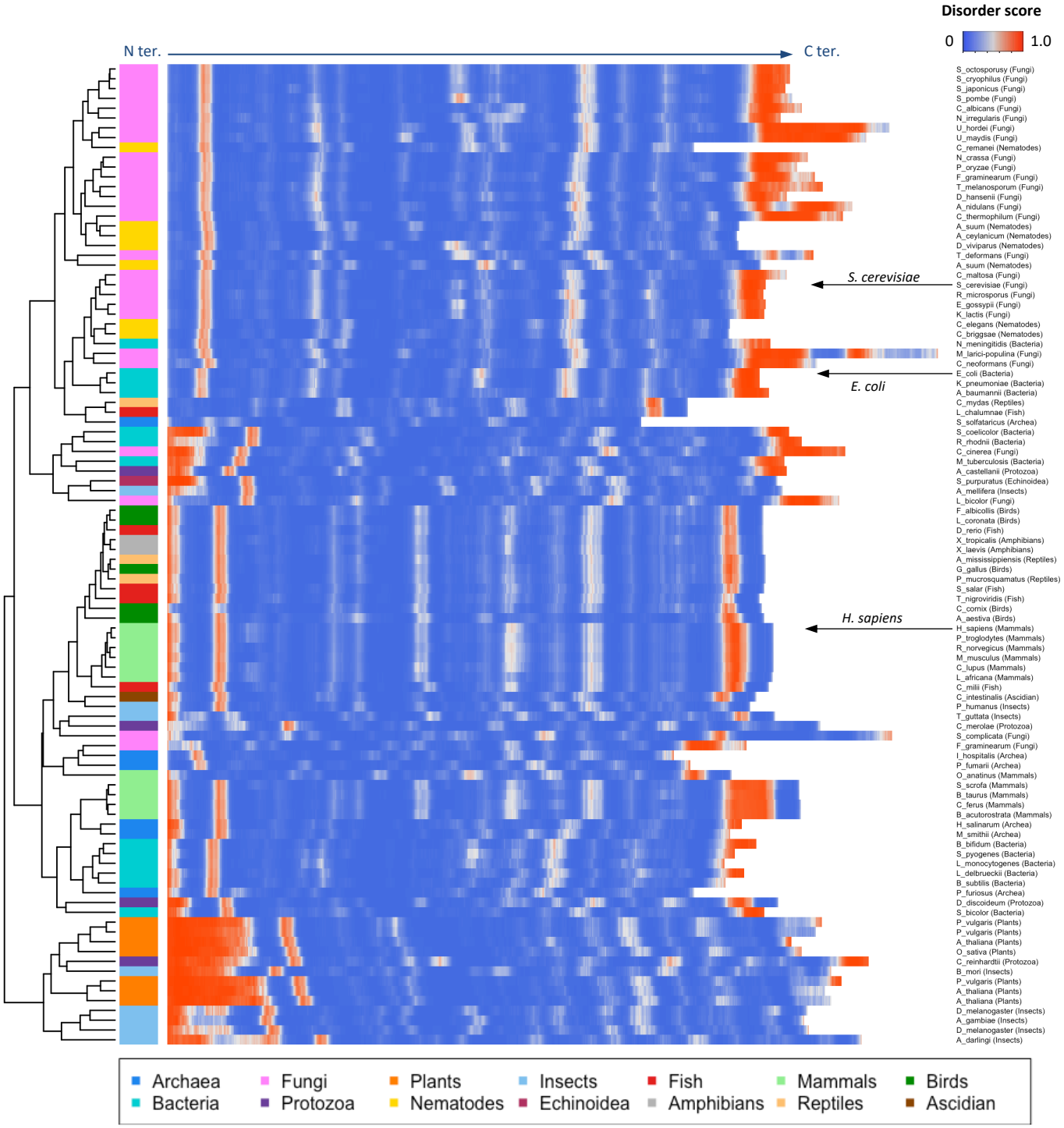

Figure 2S3: Amino acid sequences of IDRs vary across species

A

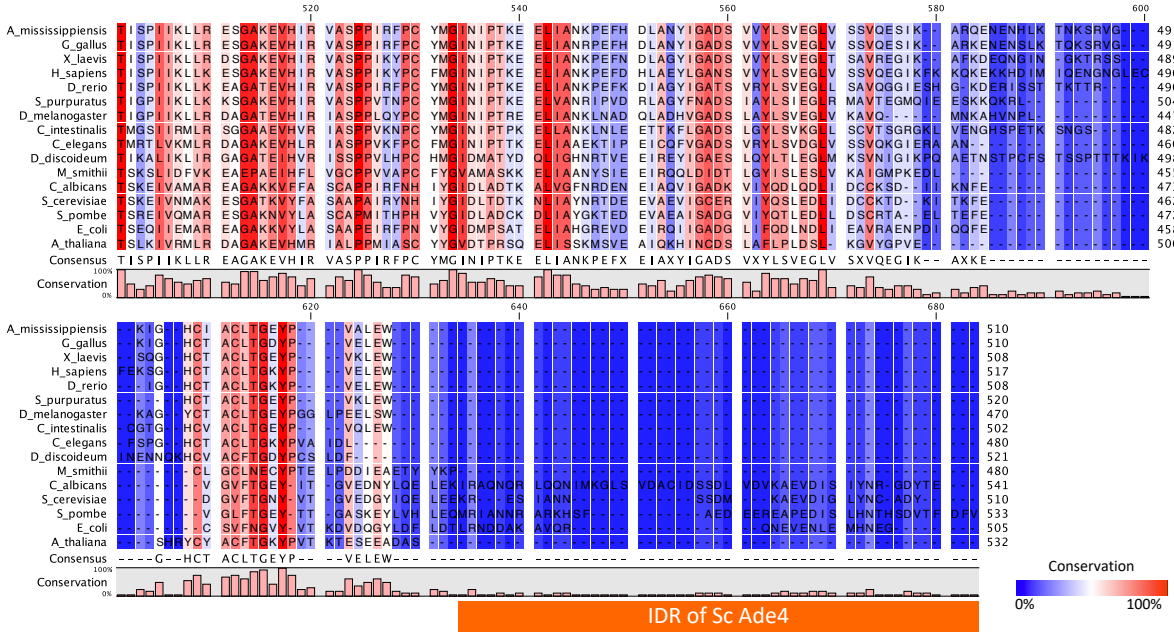

B

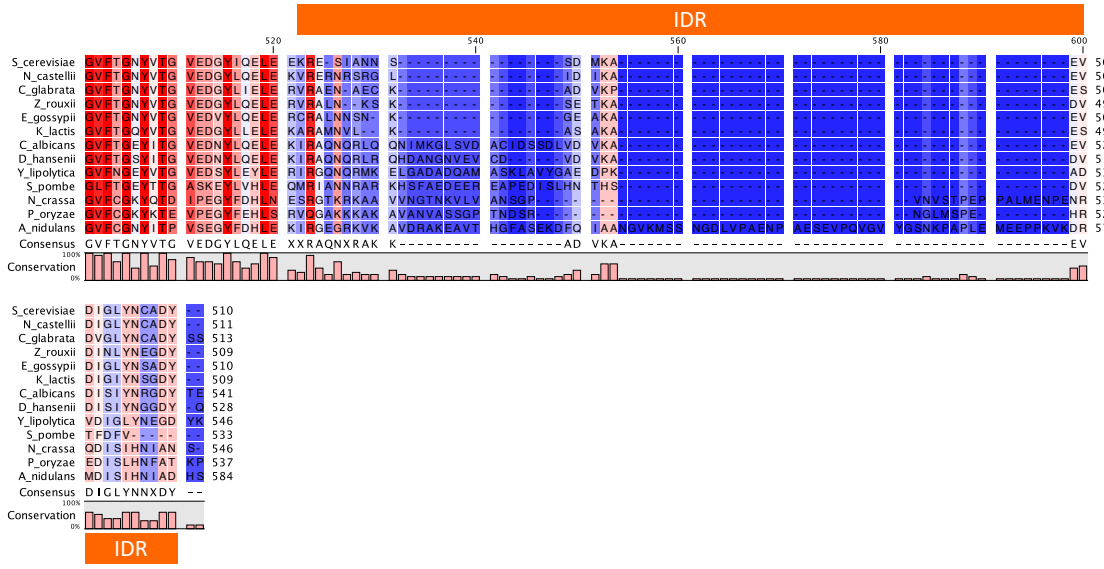

Figure 3: Formation of Ade4 granules requires active TORC1 and ribosome biogenesis

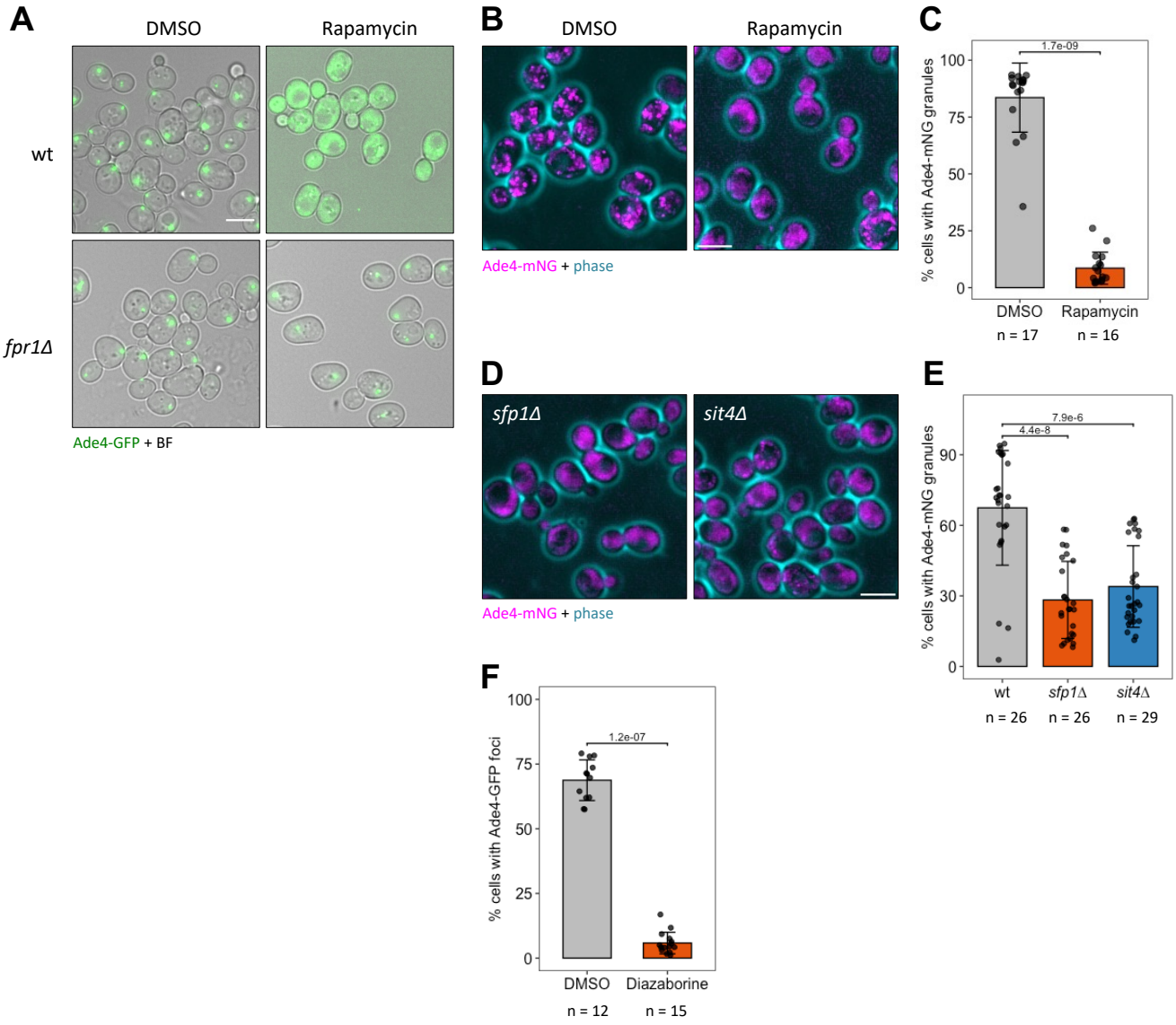

Figure 3S1: Formation of Ade4 granules in TORC1-related mutants. Related to Figure 3

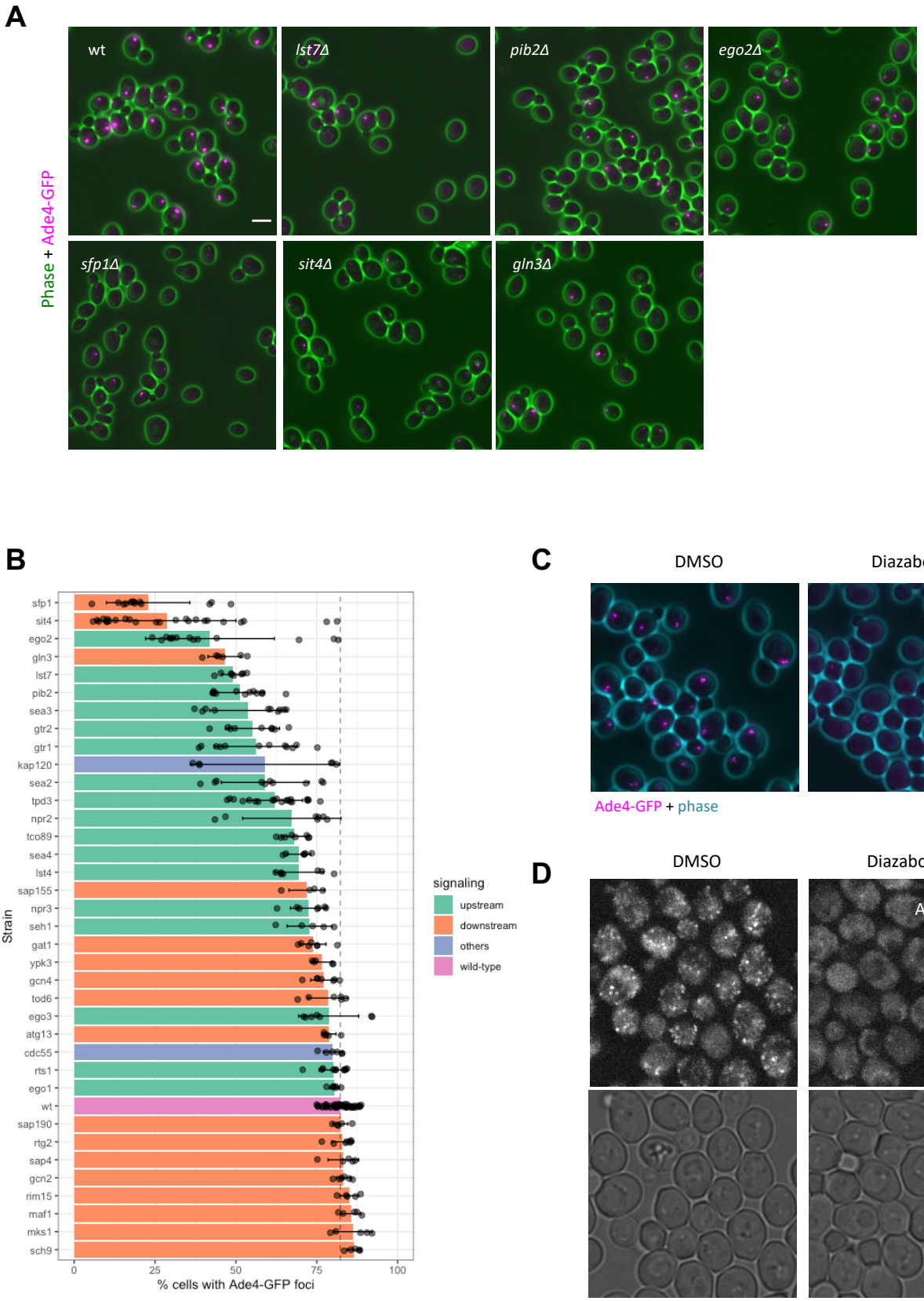

Figure 4: Intracellular derivatives of purine nucleotidse prevent the formation of the Ade4 condensates

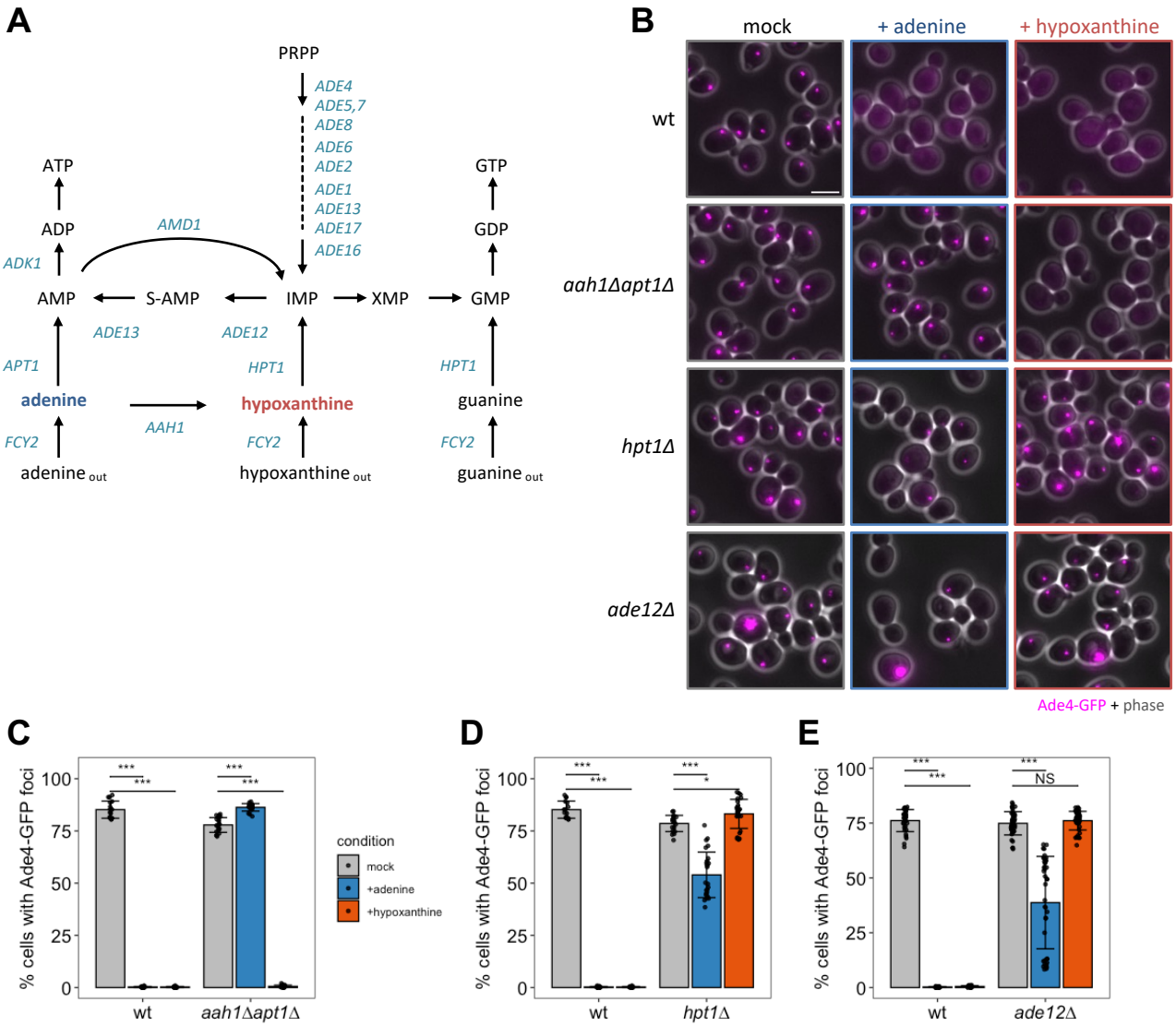

Figure 4S1: Alanosine inhibits the dissolution of the Ade4 foci in the presence of hypoxanthine

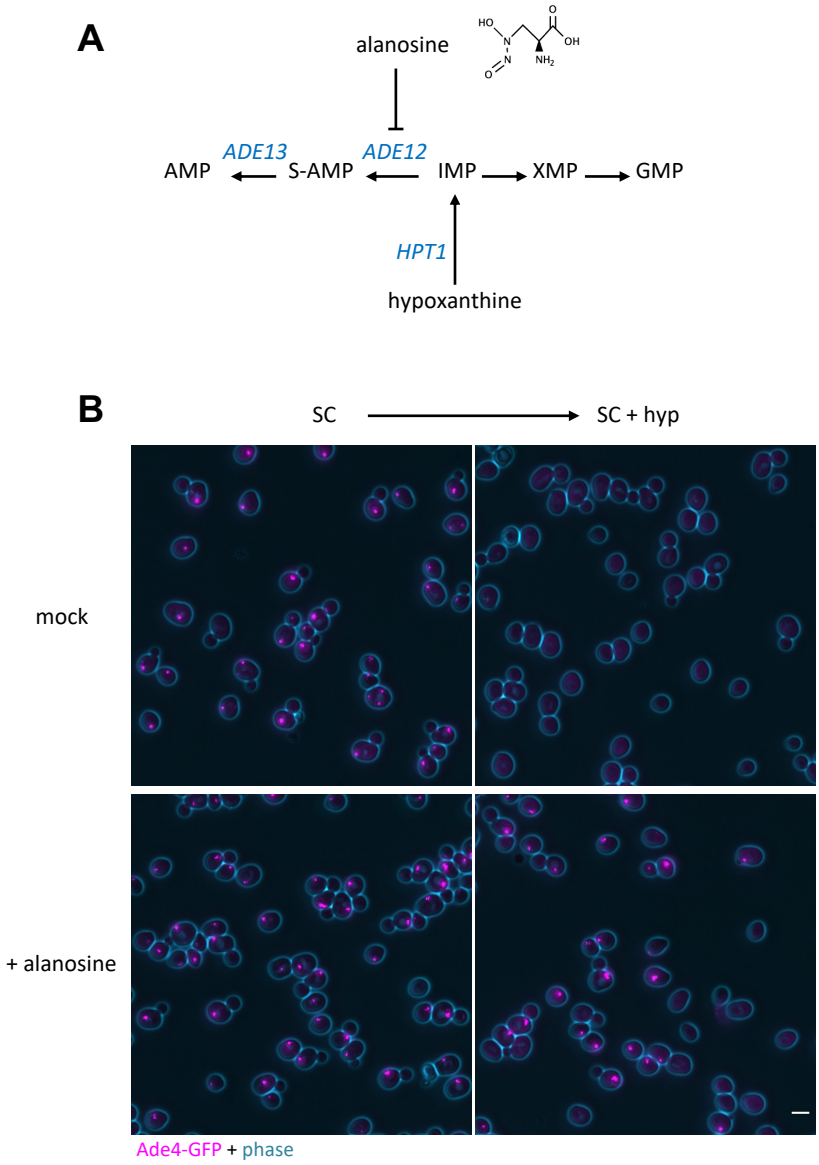

Figure 5: The interaction of purine nucleotides with Ade4 is implicated in the granule assembly

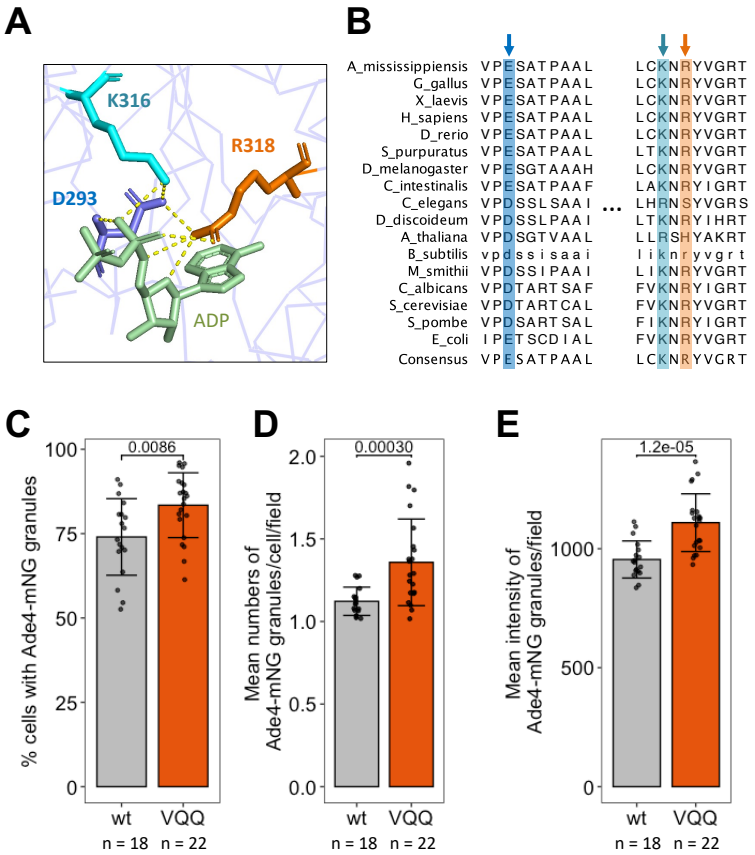

Figure 6: The Ade4 protein condensates into particles under molecular crowding conditions *in vitro*

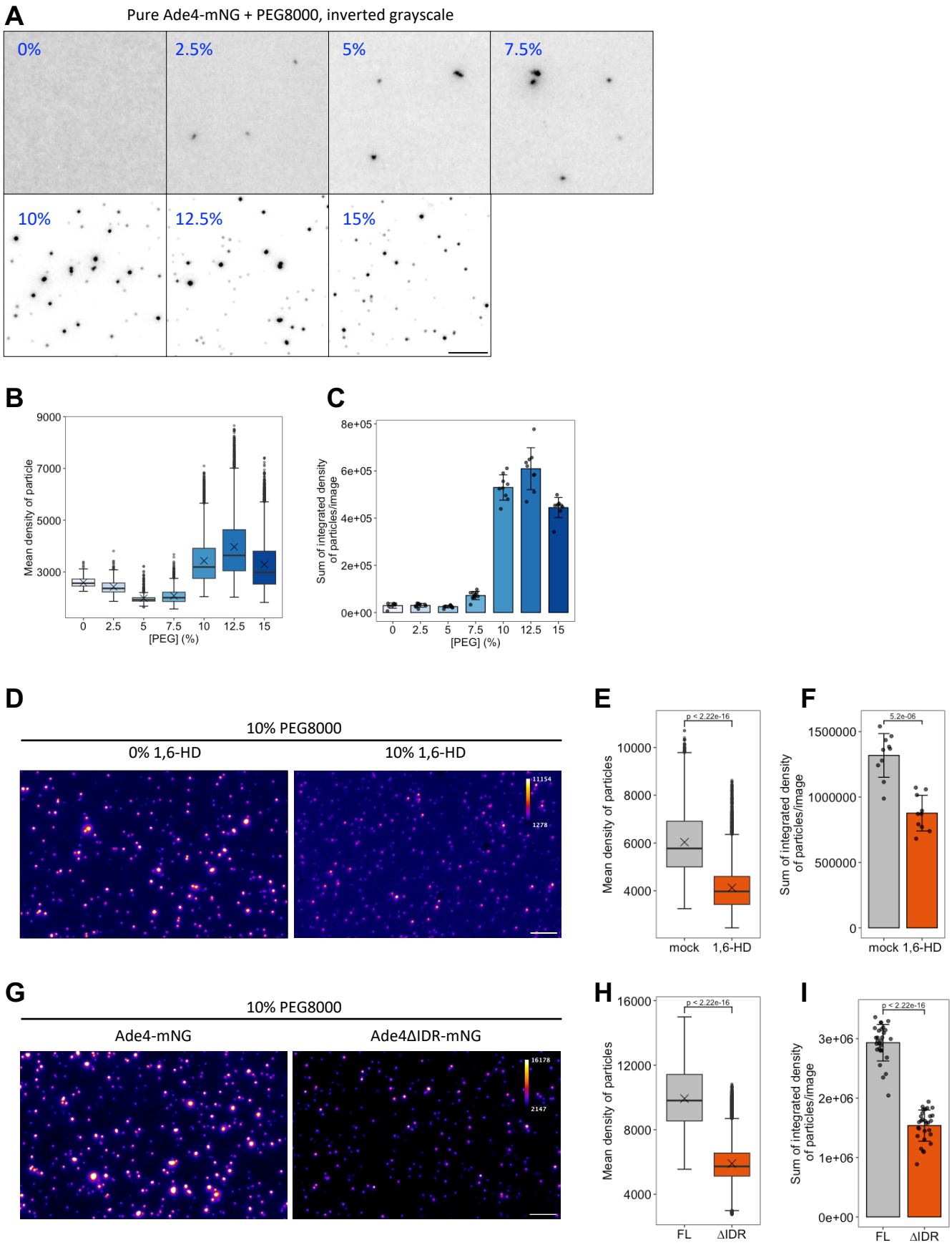

Figure 6S1: Purification and basic characterization of the Ade4 protein *in vitro*

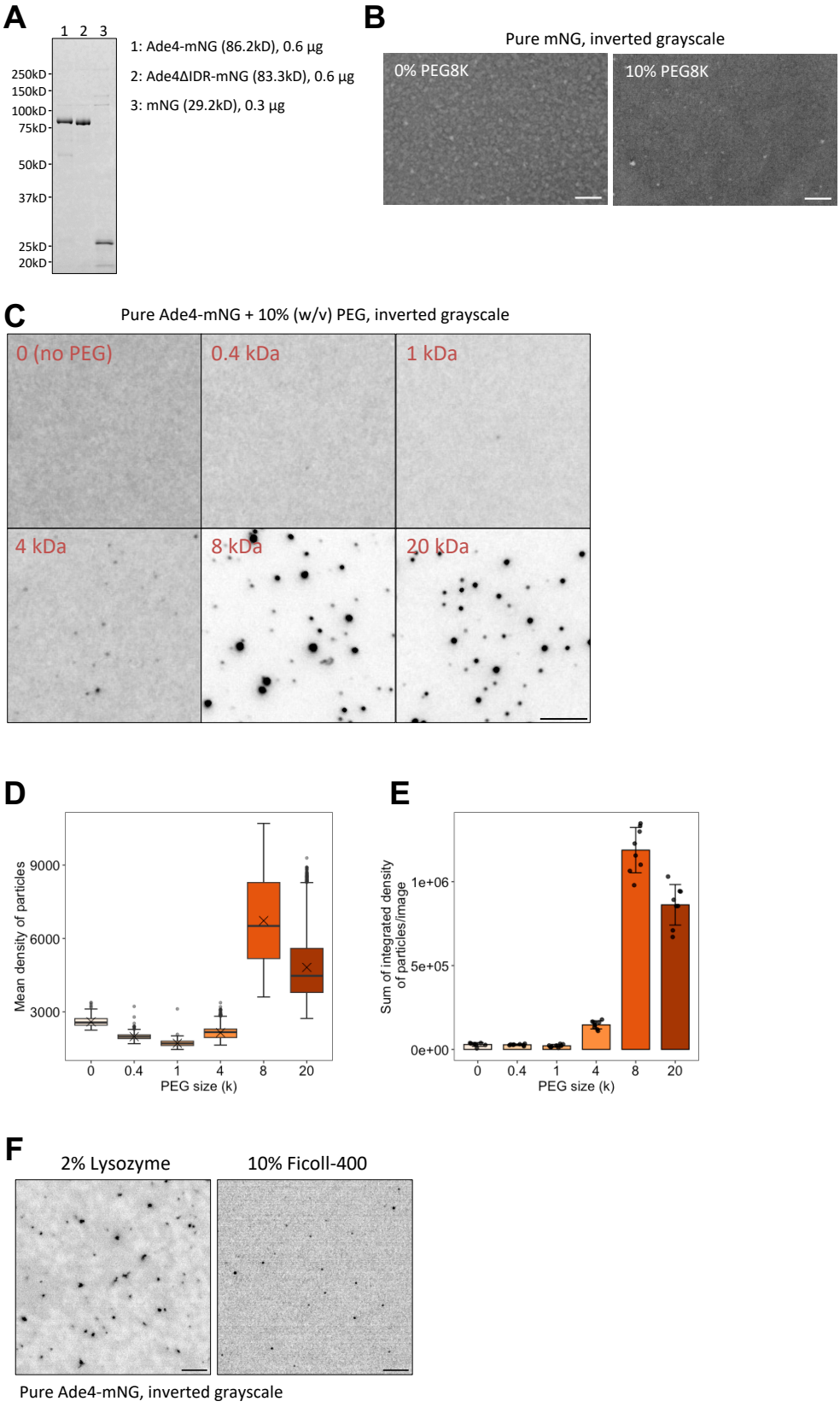

Figure 6S2: Estimation of the intracellular concentration of Ade4

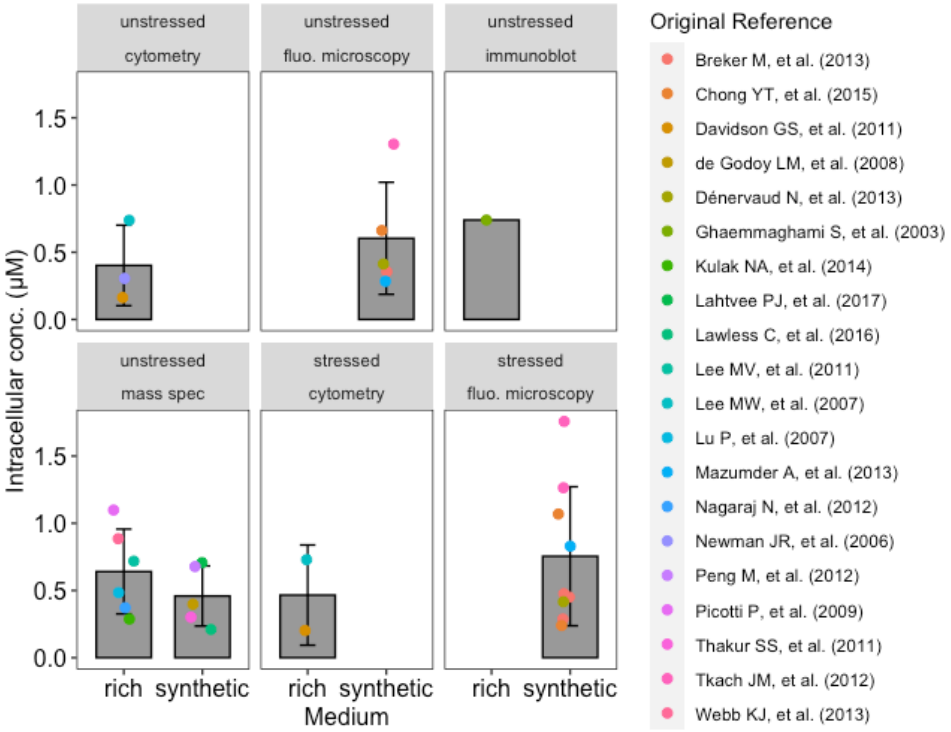

Figure 7: Purine nucleotides attenuate the assembly of the Ade4 particles *in vitro*

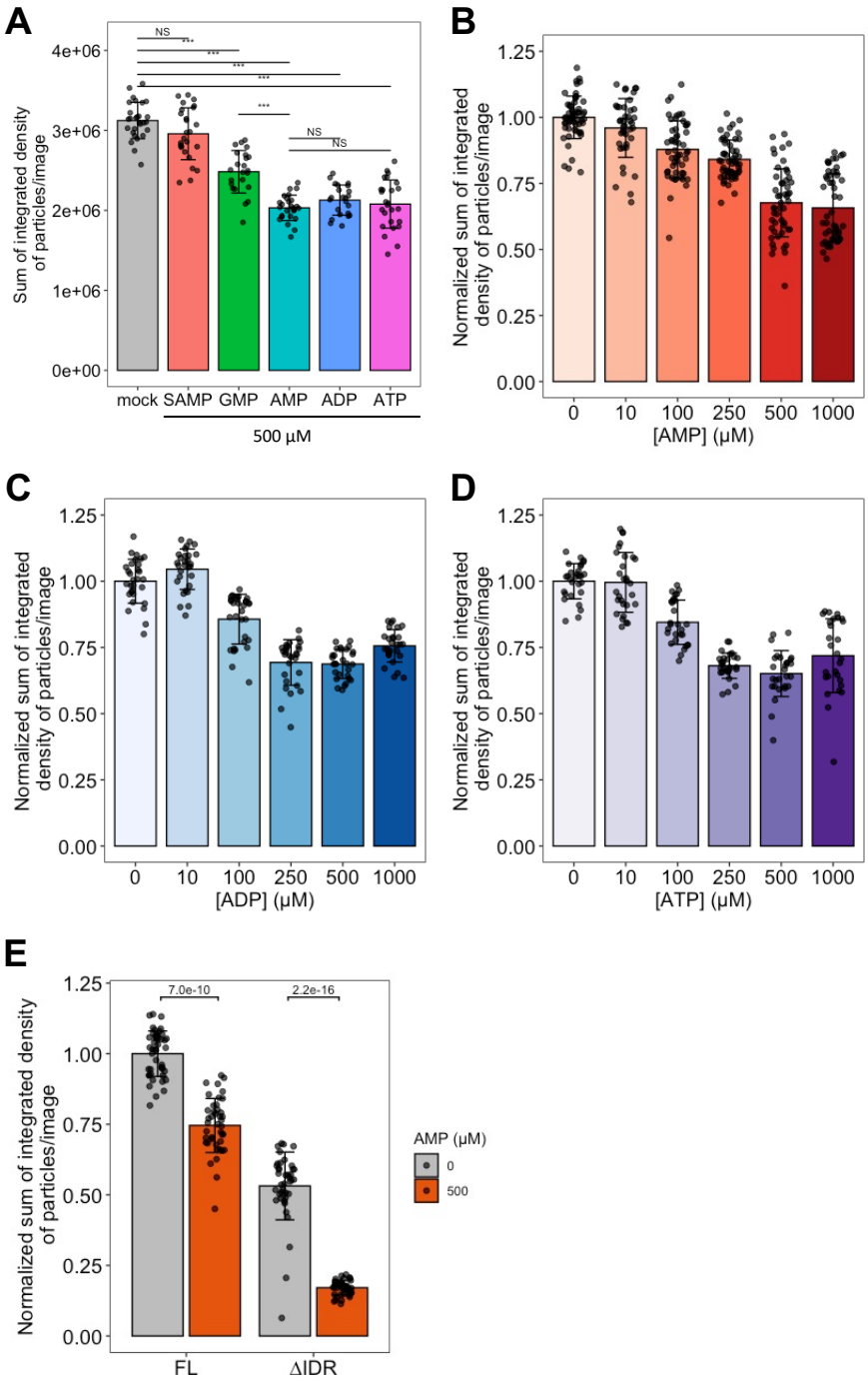

F

Condition 1:
Cytoplasmic macromolecular crowding

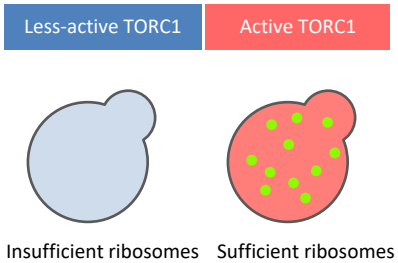

Condition 2:
Inhibitory interaction with purine nucleotides

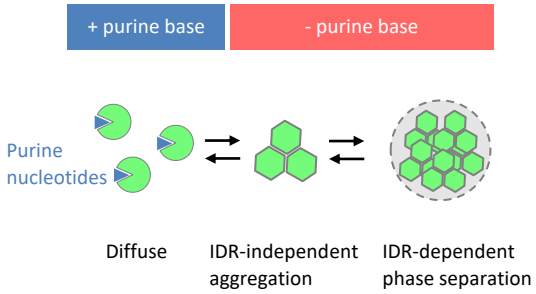

Figure 7S1: Additional data regarding the assembly of the Ade4 particles *in vitro*, related to Fig. 7

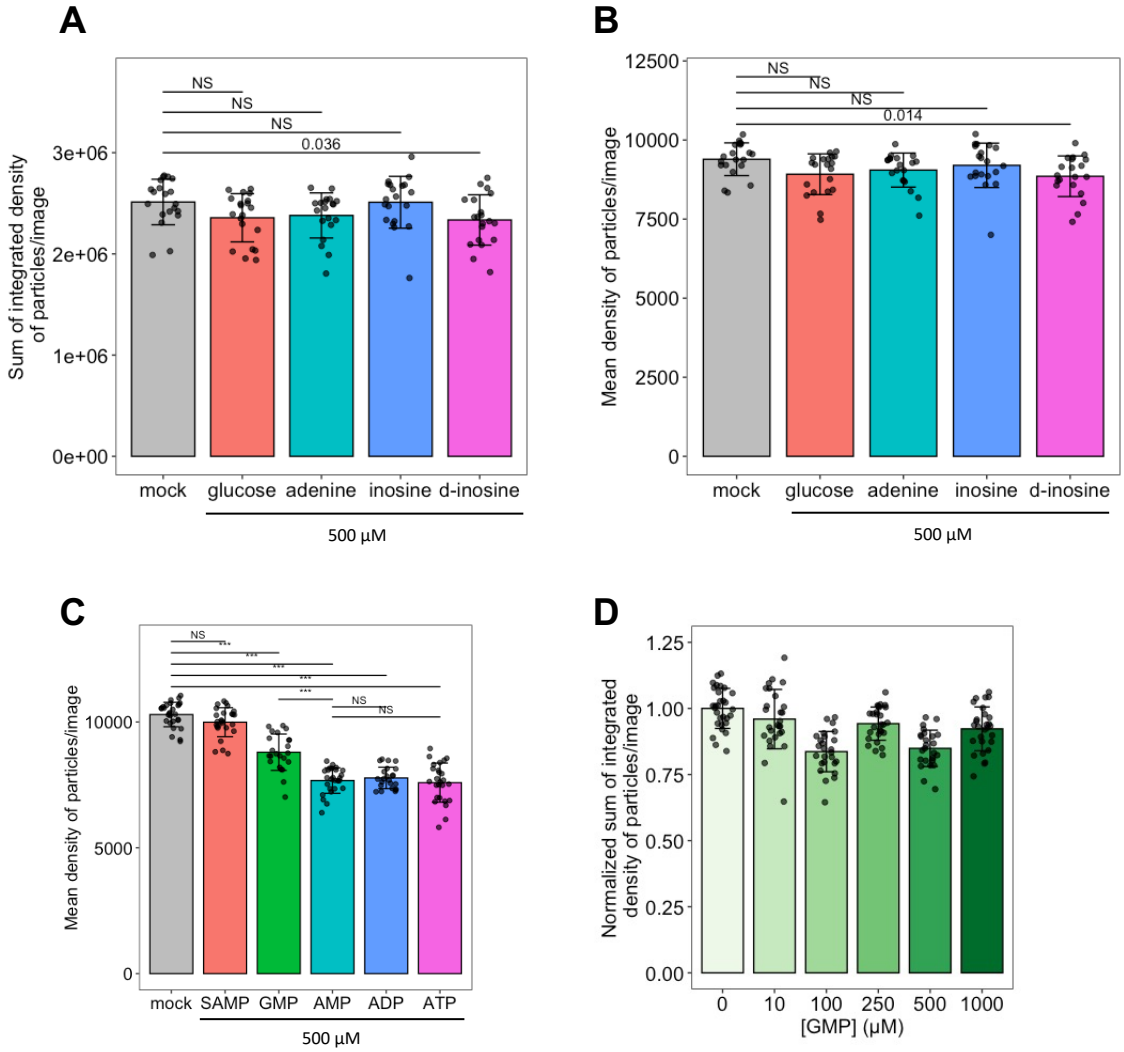

Figure 8: The formation of the Ade4 granules is important for efficient *de novo* purine synthesis during cell growth

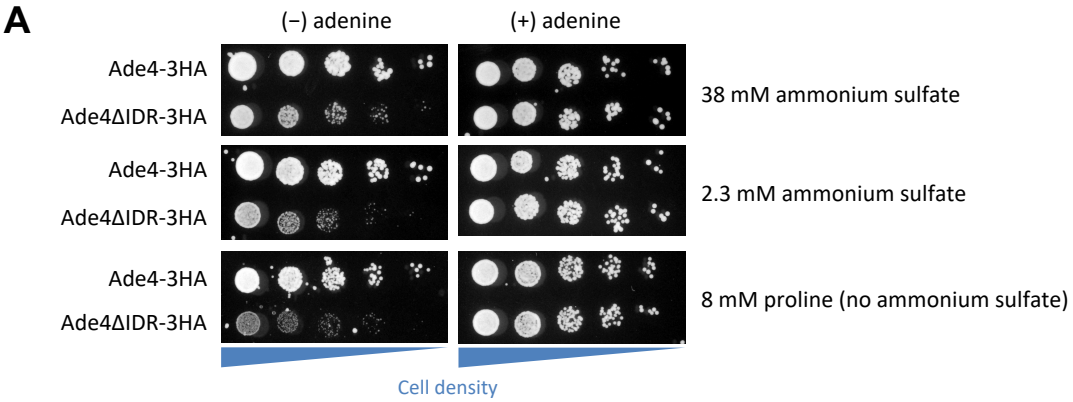

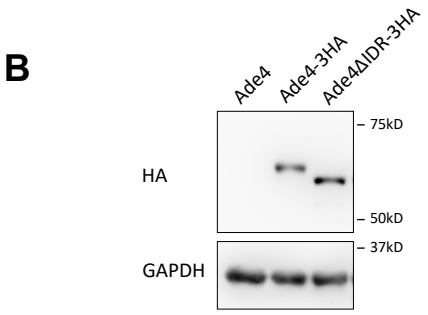

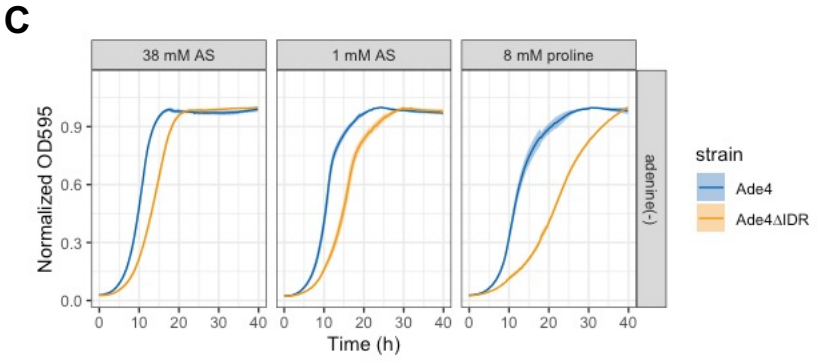

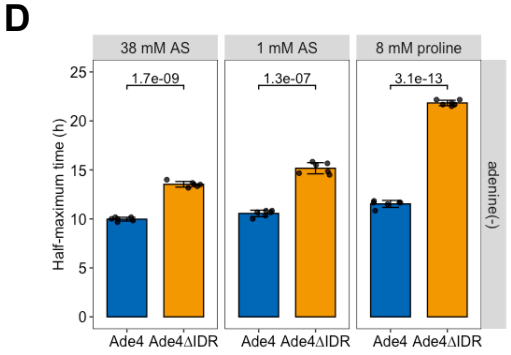

Figure 8S1: Cell growth assay in the presence of external purine bases , related to Fig. 8

A

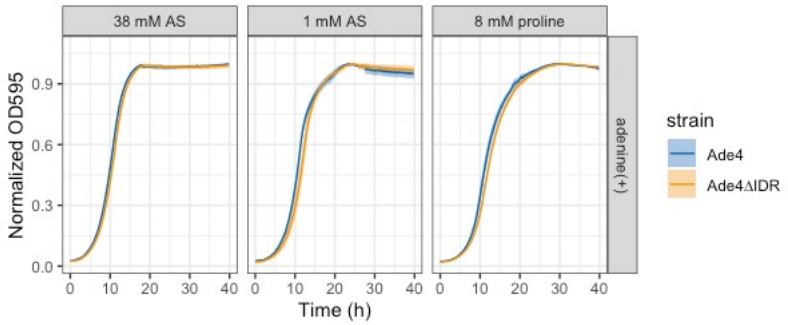

B

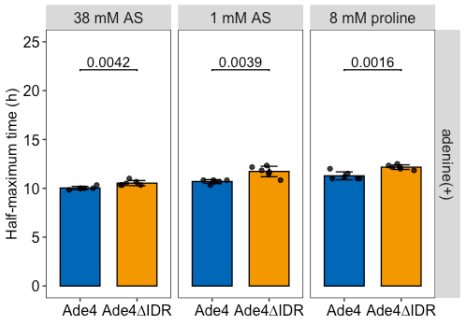

C

Gln-PRA activity:
PRPP + Gln + H_2O → PRA + Glu + PP_i

NH_3-PRA activity:
PRPP + NH_3 → PRA + PP_i

D

	Gln-PRA	NH_3-PRA
Low NH_3	Up	Down
High NH_3	Down	Up

Figure 9: MD calculations predict the potential leakage of glutamine-derived NH_3 from PPAT molecules

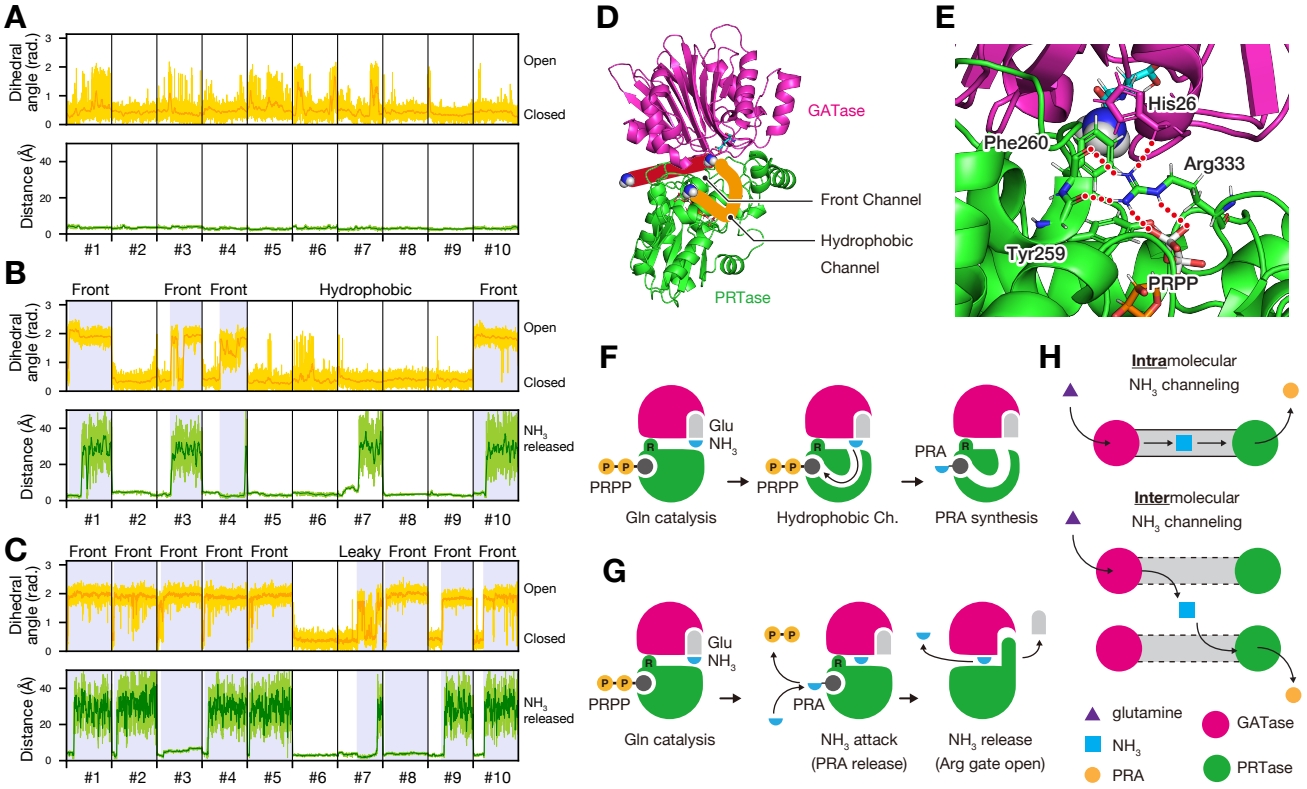
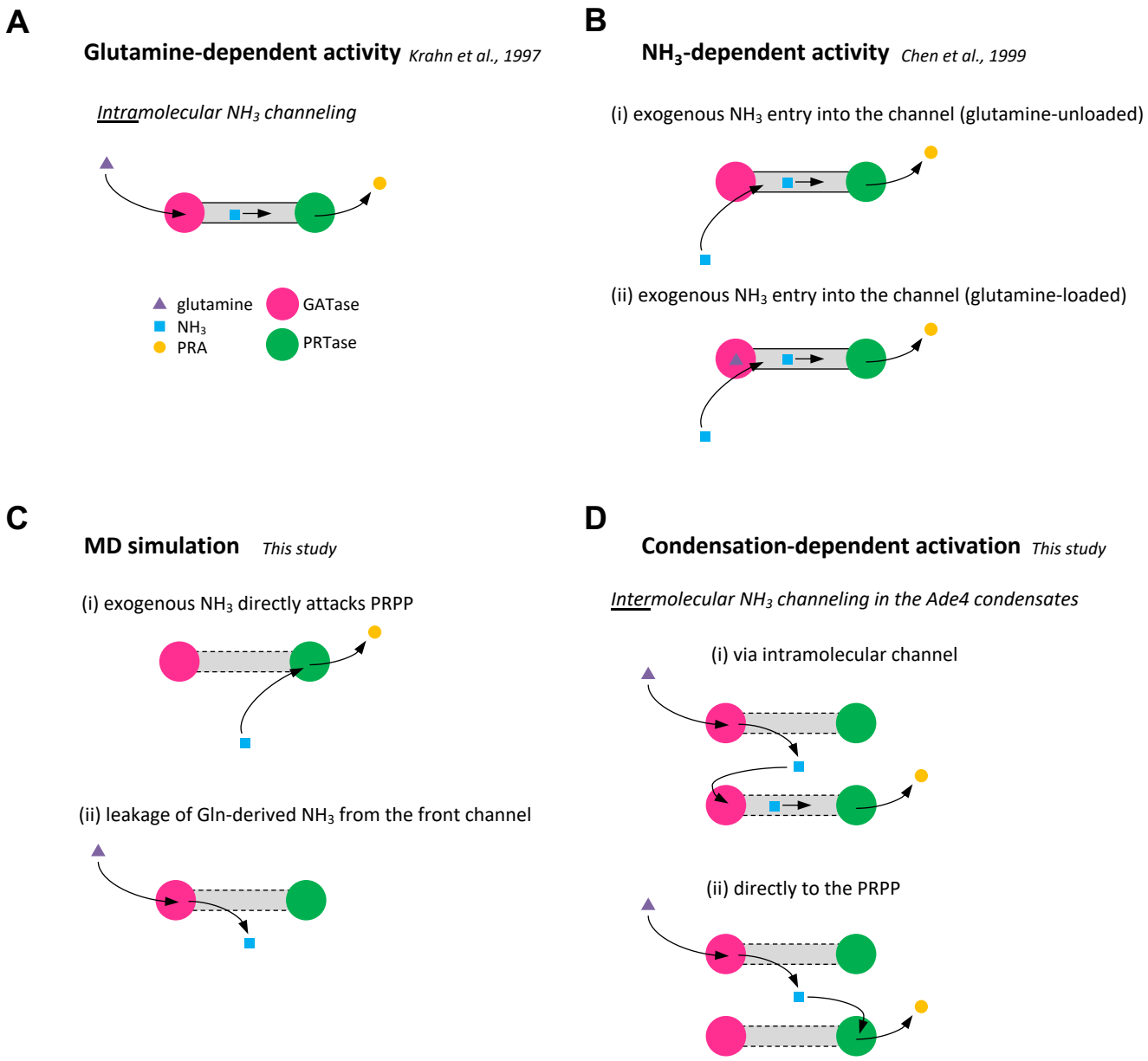
Figure 9S1: Possible enzymatic reaction pathway of PPAT